



AALBORG UNIVERSITY
DENMARK

Master's Thesis in Energy Engineering,
Mechatronic Control Engineering

Modelling, Optimisation, and Design of Fast Switching Solenoid Valve

Author

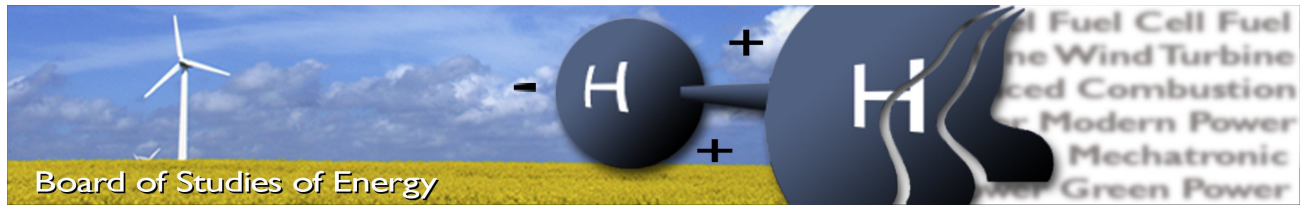
Torben Ejnar Løvbjerg Jørgensen

Supervisors

Assoc. Prof., Michael Møller Bech
PhD Fellow, Christian Nørgård



July 2017



Title: Modelling, Optimisation, and Design of Fast Switching Solenoid Valve
Semester: 10th, Master's Thesis
Project period: 01.02.17 to 01.06.17
ECTS: 30
Supervisor: Assoc. Prof., Michael Møller Bech
 Ph.D. Fellow, Christian Nørgaard
Project group: MCE4-1022

Torben Ejnar Løvbjerg Jørgensen

Pages, counting (total): 55 (63)
 Appendix: 2

Synopsis:

The transmission of large scale wind turbines has traditionally been done mechanically but the development of larger turbines has been pushing this solution to its limits and the hydrostatic transmission is candidating its dominance. However, the hydrostatic transmission has its disadvantages in that traditional hydraulic pumps and motors are inefficient at small displacements and further development is therefore needed.

Digital Displacement Technology could be the improvement needed for feasibility and has been investigated by industry and academia alike. Studies have shown that a low pressure drop and fast switching valves are necessary for the success of this technology. This thesis investigates the modelling, optimisation, and design of such valve. The valve topology of interest is the variable reluctance or solenoid valve which history has proven reliable but suffering from a poor transient response compared to newer topologies. This disadvantage is sought minimised.

The study showed showed that in order to achieve the low pressure drop necessary the travel distance must also increase causing the switching time to increase thereby yielding an inefficient design.

By signing this document, each member of the group confirms that all group members have participated in the project work, and thereby all members are collectively liable for the contents of the report. Furthermore, all group members confirm that the report does not include plagiarism.

Preface

This thesis has been carried out at the Department of Energy Technology, Aalborg University in the Spring of 2017 with funding from the HyDrive research project.

I would like to thank my supervisors Christian Nørgård and Michael Møller Bech. Without their expertise and immense interest in the project it would not have come to the fulfilment it has. I would also like to thank the institute workshop, for not only machining the valve in excellent quality but also fruitful dialogue, both early and late in the design phase, about the machining technique and foresight of issues and challenges which could be pre-emptively solved.

Reading Guide

The reader should have a basic knowledge of calculus as well as a good understanding of electromagnetic system modelling and fluid dynamics.

The nomenclature and abbreviations used through out the report is presented in the beginning of the report.

The Vancouver referencing system is used, where a number in square brackets is presented in the text referring to the bibliography. Additionally, page number is stated for specific references in references within the square brackets.

Chapters, section, tables, figures, and equations in the report are refereed to by the object in hand followed by the object's number number. For instance, the 14th figure in Chapter 3, would be refereed to by "Figure 3.14".

Contents

1	Introduction	1
1.1	Wind Turbine Drivetrains	1
1.2	Digital Displacement Machine	2
1.3	State of the Art Valves for Digital Displacement Machines	3
1.4	Pole Shaping	6
1.5	Problem Statement	9
2	Modelling	11
2.1	Digital Displacement Machine	11
2.2	Electro Magnetic Modelling	15
2.3	Fluid Mechanic	18
2.4	Mechanical Stress Considerations	24
3	Optimisation	27
3.1	Object Functions	27
3.2	Design Variables	30
3.3	Optimisation	30
3.4	Optimisation Results	32
4	Experiment	35
4.1	Prototype	35
4.2	Experimental Setup	37
4.3	Experiment Results	37
5	Conclusion	41
	Bibliography	41
A	Modelling	45
A.1	Electromagnetic Characteristic Mapping	45
A.2	Coil Characterisation	46
A.3	Mesh Dependence for Numerical Methods	48
B	Test population	51

CONTENTS

1 | Introduction

Wind turbines play a key role in the current global search for green solutions to satisfy the growing energy needs. However, harvesting the energy of the wind is not a new concept and can be traced back to first century Greece where Heron of Alexandria used a wind-driven wheel to power an organ[2]. In more modern times wind mills were used as a tool to grind wheat and other grains into flour and pumping groundwater to the surface. Nowadays, wind turbines are primarily used to generate electricity for the common electrical grid both onshore and offshore.

1.1 | Wind Turbine Drivetrains

The drivetrain of large scale horizontal axis wind turbines consist of the blades, transmission, generator, and converter. Three different types dominate the commercial market for large scale wind turbines [9].

- **Directly driven generator with full power converter:** With the blades directly connected to the generator shaft, the mechanical transmission is omitted, however, the generator turns slowly and therefore needs more poles thereby increasing the size of the generator. The generator is then connected to a full power back-to-back converter meaning all the power generated by the turbine goes through the converter. The advantage of this type is the lack of a mechanical transmission which thereby limits the number of moving parts and thereby the possible points of failure.
- **Medium ratio gearbox and full power converter:** This type is much like the first type, however, the blades and the generator are connected by a fix ratio gear box which increases the generator shaft speed in turn lowering the number of poles needed. However, it has more moving parts which are prone to failure.
- **High ratio gearbox and doubly-fed induction generator:** This type has a gearbox, which can change its gearing ratio, thereby allowing the blade shaft to turn at different speeds and the generator to have an electrical speed equal to that of the common grid. This means that the generator can be directly connected to the common grid consequently lowering the requirements of the converter which only purpose is regulate the speed of the generator. Typically these converters have a power rating at about 25 % that of the turbine.

These three types have different advantages and disadvantages with all being actively used commercially by companies such as Siemens and Vestas. However, a disadvantage for the second and third type is the mechanical transmission which, as turbines increase in capacity, are prone to more stress.

Therefore, alternative transmission types may be candidates to replace the mechanical transmission in the future. One such alternative transmission is the hydrostatic transmission which uses a combination of a hydraulic pump and hydraulic motor to change the output shaft speed. This results in the blade shaft and the generator being decoupled mechanically. Hydraulic solutions are of special interest since they are often associated with a high power density. However, traditional hydrostatic transmissions, such as the swash-plate and bent-axis types, suffer from poor efficiency at low displacements and therefore further development must be made for this alternative to be feasible.

Digital Displacement Technology (DDT) transmission is a promising alternative to counter this inefficiency at low displacements. It consists of two Digital Displacement Machines (DDM). One is connected to the blade shaft and is responsible for pumping oil from the low pressure manifold to the high pressure manifold, and the other is responsible for turning or motoring the generator shaft by letting oil pass through the chamber from the high pressure to the low pressure manifold. A more elaborate description of the DDM will be presented in the following section.

1.2 | Digital Displacement Machine

The DDM consists of multiple chambers which are connected to the Low Pressure Manifold (LPM) via a Low Pressure Valve (LPV), the High Pressure Manifold (HPM) via a High Pressure Valve (HPV), and the central shaft via a piston as seen in Figure 1.1. These chambers are spread around and along the central shaft as seen

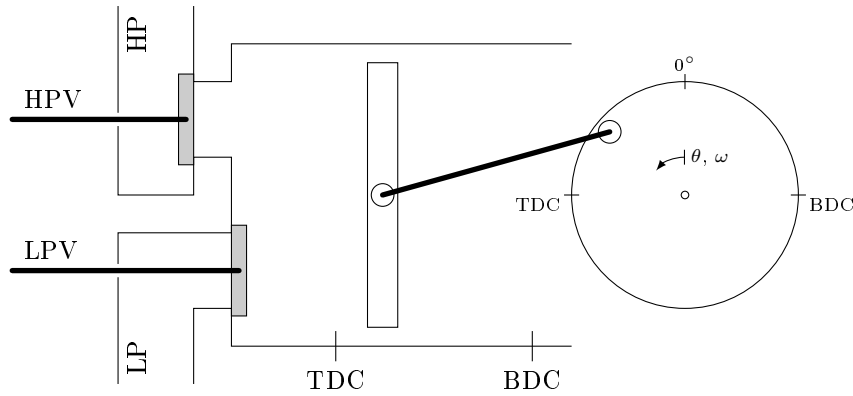


Figure 1.1: Sketch of a single DDM chamber.

for the motoring DDM in Figure 1.2. Each chamber can be operated individually and through a single shaft revolution each piston will or will not exert a torque on the central shaft depending on the operation mode. The

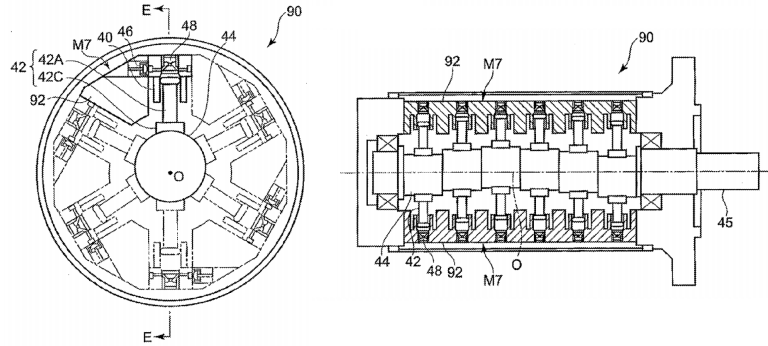


Figure 1.2: Digital displacement motor with six pistons around the shaft and six rows along the shaft from [12]. 42 is the piston, 46 is the HPV, and 48 is the LPV.

chambers of the pump can operate in pump mode or idle mode, and the chambers of the motor can operate in motor mode or idle mode. The specific operation mode is determined by the specific valve sequence for each chamber. This thesis will focus on the motoring DDM which operates in either idle or motoring mode dependent on how much displacement is wanted at the moment. Idle mode is the simpler of the two where the LPV is always open meaning the oil enters from the LPM and exits to the LPM. Motor mode is slightly more complicated. Starting with the LPV open and the HPV closed the chamber is contracting meaning the piston is

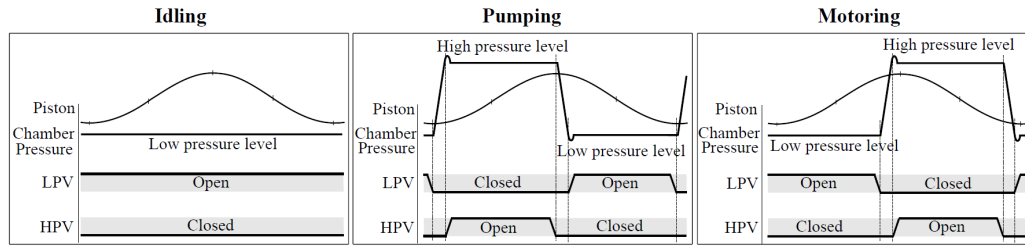


Figure 1.3: The three operation modes of the digital displacement machine. [9, p. 13]

moving towards the Top Dead Centre (TDC). Before it reaches this point the LPV closes actively, meaning the actuator part of the LPV exerts a closing force, leaving the chamber closed and contracting thereby increasing the pressure. When the pressure exceeds that of the HPM the HPV will passively open, meaning no actuator force is needed, and the piston will pass TDC and start expanding. With the piston expanding by moving towards the Bottom Dead Centre (BDC) the HPV must close actively before reaching this point. When the HPV has closed, the chamber is again closed but now expanding thereby lowering the pressure until it surpasses below that of the LPM causing the LPV to passively open. The piston now reaches the BDC and the cycle continues.

With the valves being such a significant component of the DDM a low pressure drop and fast switching time is essential for efficient operation and thereby for the DDM to be feasible. Requirements and proposals for these valves will be described in the following section.

1.3 | State of the Art Valves for Digital Displacement Machines

The valves needed for efficient operation must have a low pressure drop and a short switching time as seen in Figure 1.4. However, achieving both a low pressure drop and fast switching time may prove difficult since a low

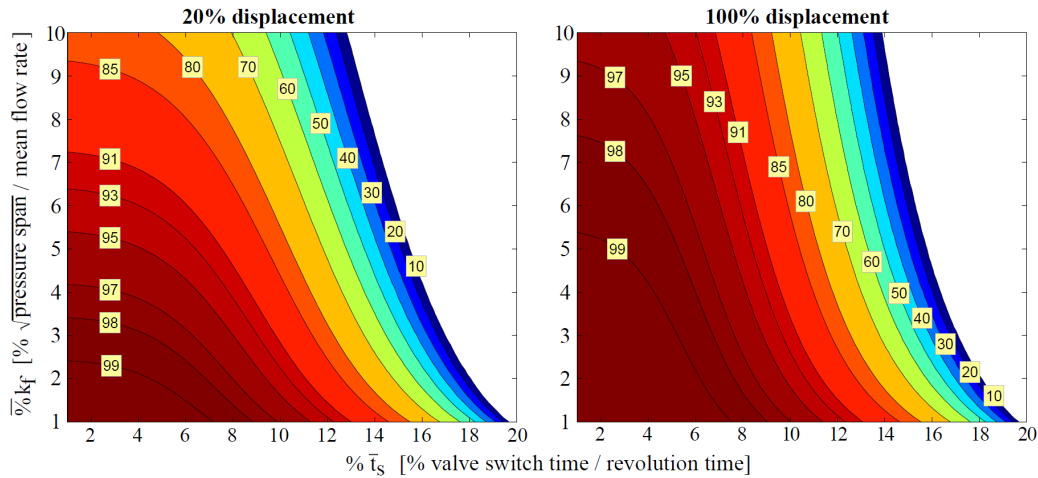
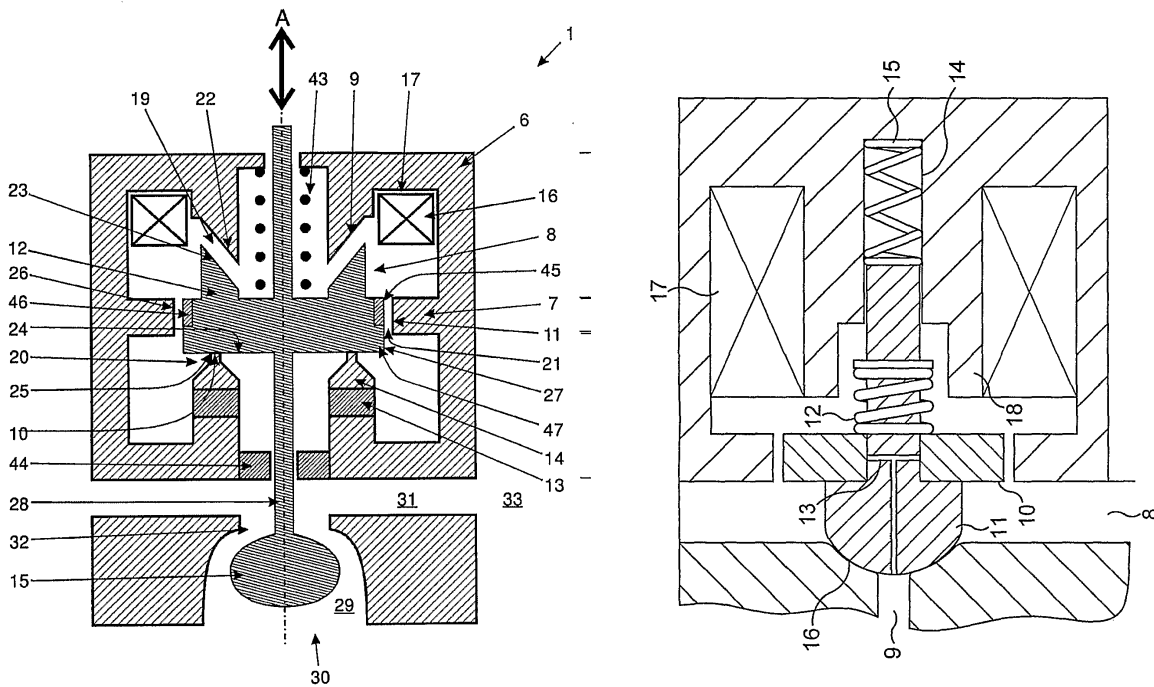


Figure 1.4: Correlation between pressure drop and switching time, and the DD motor efficiency at 20 % and full displacement. [9, p. 46]

pressure drop typically is associated with a large discharged area which is associated with a large valve travel distance and thereby a slow switching time. Therefore, the ideal valve is a trade-off between a low pressure drop and a fast switching time.

The concept of DDT has been studied for many years by companies such as the leading company Artemis Intelligent Power which was formed in 1994 to ... *develop the next generation of hydraulic machines using Digital Displacement® Technology*. In 2010 the company became a subgroup of Mitsubishi Heavy Industries and in 2014 erected the 7 MW Mitsubishi Sea Angel outside Hunterston, Scotland. [7] However, it is not yet commercially viable. Other studies have been made by Aalborg University in collaboration with Johannes Kepler University in Linz and others as part of the HyDrive project. [1] Other universities such Tampere University of Technology and Purdue University are also actively investigating future applications of digital hydraulics.

Artemis's valve actuator patents operate using variable reluctance as seen in [8] and [10]. The variable reluctance or solenoid topology has proven historically to be a robust and reliable actuation method in-part due to its simplicity. However, it struggles with having a poor transient response partially because all magnetic flux is



(a) Sketch of Artemis valve by William Rampen from 2011 [8] (b) Sketch of Artemis pilot valve by Uwe Stein from 2014 [10]

Figure 1.5: Two of Artemis's valve designs which have been patented.

generated by the coil. Artemis has tried to circumvent this drawback by adding permanent magnets (13) in 1.5a, or by not directly actuating the entire plunger, i.e. pilot valve.

However, newer topologies with better transient response exist and has been assessed as part of the HyDrive project with promising results as seen in Figure 1.6. In that study the variable reluctance design proposed was not optimal for DDT since it is capable of both opening and closing actively which is not necessary for the DDM. Furthermore, it has an unnecessarily heavy moving mass and a long travel distance both disadvantaging the variable reluctance topology, especially.

Even compensating for a more optimal design it is hard to imagine the variable reluctance topology outperforming the moving coil topology and therefore the research was continued in that direction. Further studies in a more manufacturable and less idealistic design led to the construction of a fast switching moving coil design as seen in Figure 1.7. This design has a stroke length of 2.5 [ms] and a switching time of approximately 2 [ms].

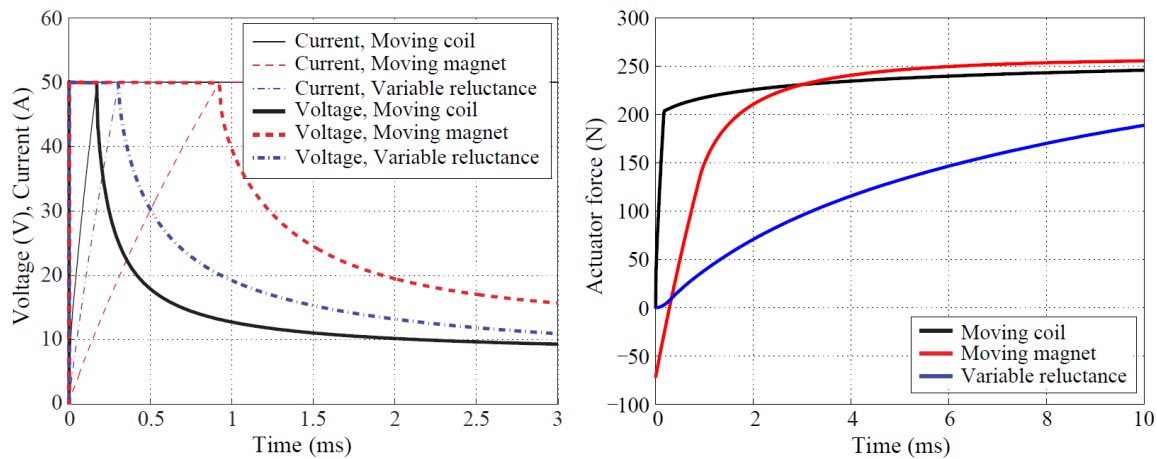


Figure 1.6: Transient response of the three topologies showing the moving coil and moving magnet outperforming the variable reluctance topology. [9]

The moving coil topology has the disadvantage that it requires a wire connecting the coil in the high pressure

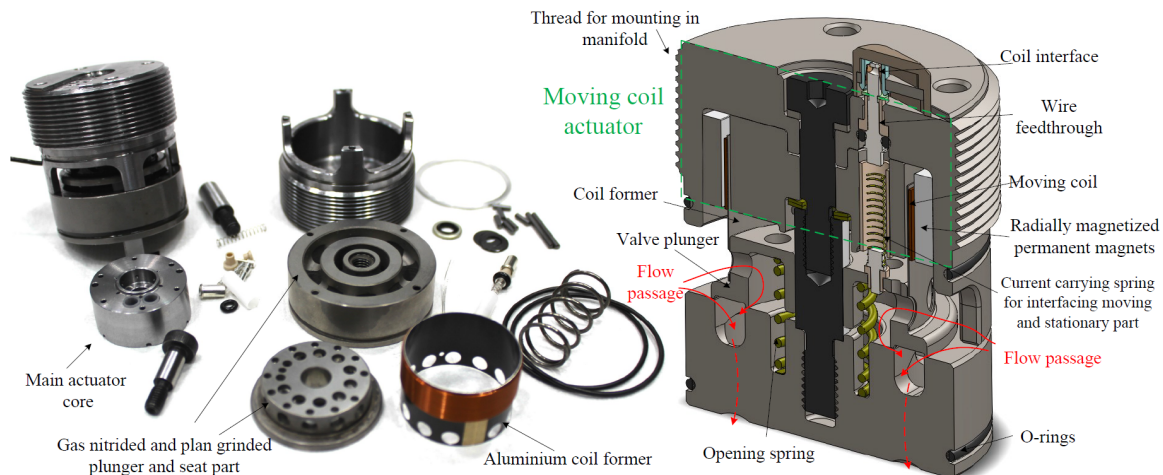


Figure 1.7: Fast switching moving coil valve which has a switching time of approximately 2 [ms] and a stroke length of 2.5 [mm]. [6]

oil and the outside atmosphere which can be difficult or at the very least be a point of potential failure.

With the variable reluctance topology being actively investigated by Artemis and the comparison discouraging it being done with parameters disfavoured it, it was further investigated during a ninth semester project at Aalborg University by the author. With a new geometry which had the purpose of lowering moving mass by incorporating the plunger into the flux path. It also decreases the travelling distance by having multiple flow paths thereby achieving the same discharge area for a shorter travel distance and can be seen in Figure 1.8. This design showed promise in that it was possible to design so that it would function. Furthermore, its simple design meant that machining, assembly was relatively simple, and no advanced components were needed such as custom made magnets or titanium components.

However, it still suffers from a long travel distance and a large pressure drop. Pole shaping, that is shaping the plunger so that the flux path and the travel of the plunger does not align, is investigated to compensate for this. This can be done by shaping the entire plunger so that it fits into the core like the cork of a bottle where the

contacting surfaces, when closed, are slanted. It can also be done by making part of the plunger overlap part of the core while keeping all contacting surfaces horizontal as done by [4]. These adaptations may help counter the travel distance disadvantage of the variable reluctance valve and will be briefly investigated in the next section.

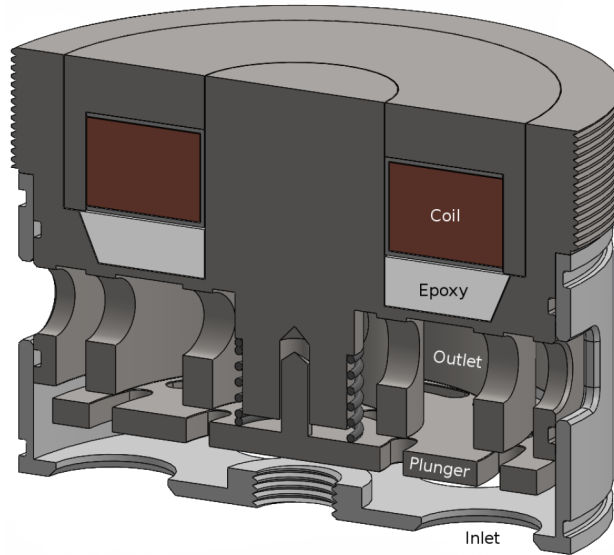
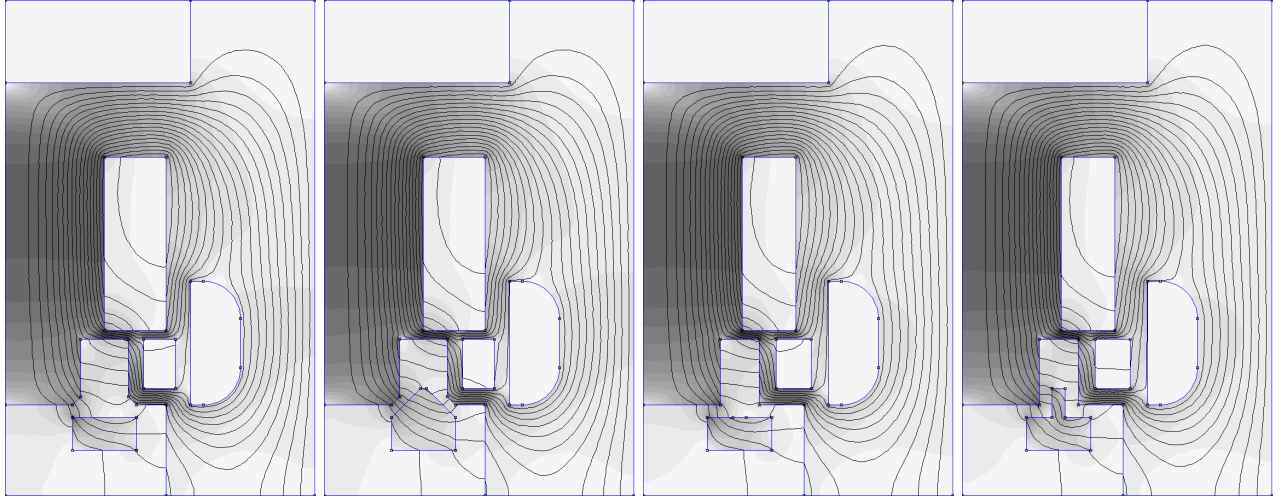


Figure 1.8: Design developed during the ninth semester.

1.4 | Pole Shaping

Two ways of pole shaping, cork and tap, has been investigated. Successfully shaping of the poles will alter the force characteristic so that the actuator force is not penalised as much for having a longer travel distance since the flux path is no longer aligned with the mechanical path of the plunger. This effect can be seen in Figure 1.9 where it is noticeable that the changed plunger shape alters the flux path.

To study this more in depth the definitions for the overlap can be seen in Figure 1.10. By keeping all other parameters constant and only varying the overlap this effect has been isolated as seen in Figure 1.11. The results thereof can be seen in Figure 1.12. It can further be seen that both geometries reach maximum force at around 0 [mm] overlap, however, the cork geometry is affected much more by the overlap than the tap geometry. This may be due to the specific design studied, however it is noticed that, especially for the tap geometry, a too large overlap acts as a magnetic short cut and exerts virtually no force on the plunger as seen in Figure 1.13.



(a) Cork geometry with no protruding. (b) Cork geometry with 2 [mm] overlap. (c) Tap geometry with no protruding. (d) Tap geometry with 2 [mm] overlap.

Figure 1.9: Affect of overlap in the extremes between it not protruding from the plunger and a 2 [mm] overlap between the plunger and core when the plunger is fully opened.

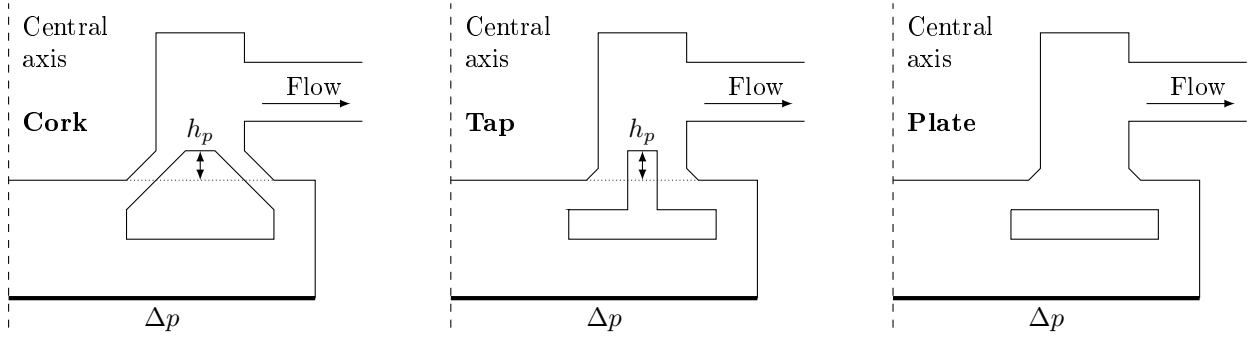


Figure 1.10: Sketch of the cork and tap topologies as well as the fundamental plate topology. These will be studied in this section to compare pressure drop and static actuator force with different overlaps, h_p .

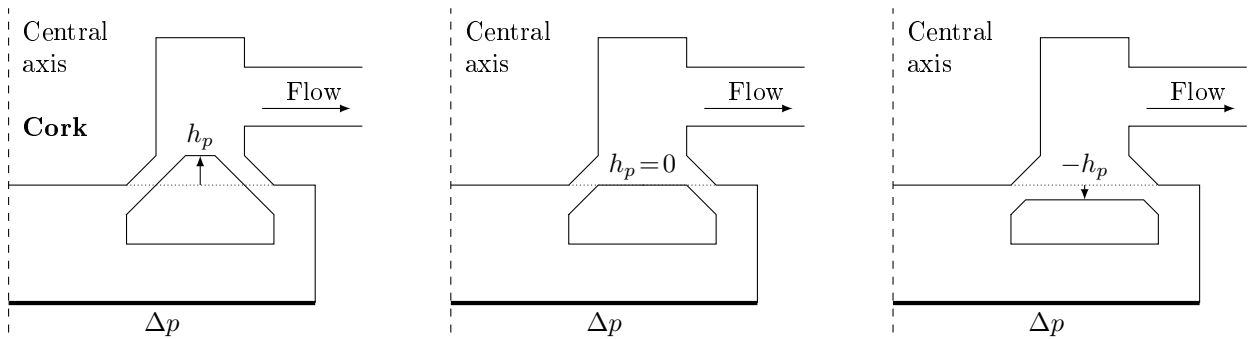


Figure 1.11: Changing of the plunger overlap parameter h_p on the cork geometry. Note that it does not change the angle of the surface which it rests on when it is closed.

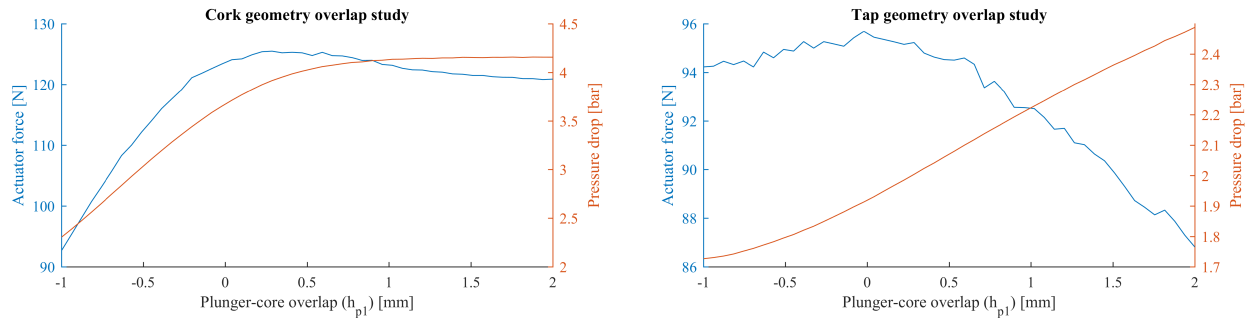
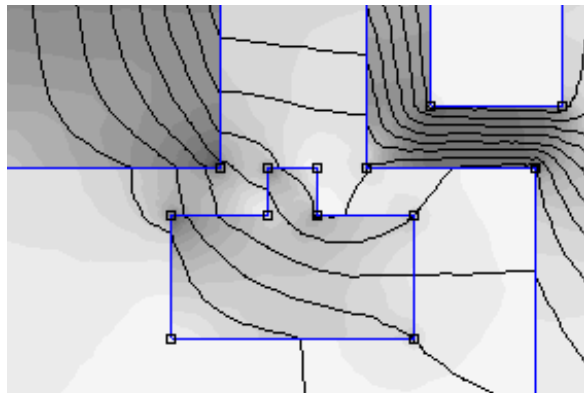
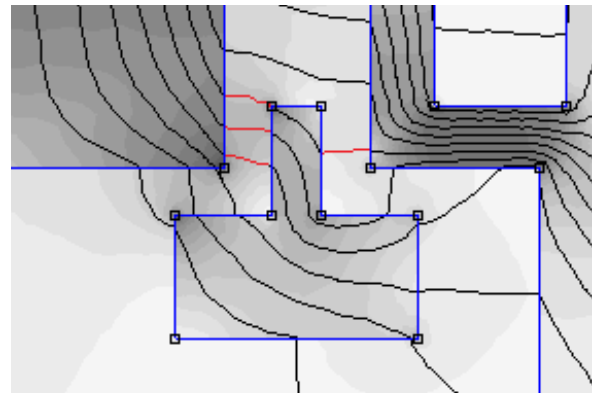


Figure 1.12: Overlap study showing a maximum force close to no overlap for both geometries, however, it is noted that the cork geometry is affected more by the overlap than the tap geometry.



(a) Tap geometry with zero overlap.



(b) Tap geometry with 2 [mm] overlap. Notice that the red lines between the core and plunger are almost entirely radial and therefore exert no force and are essential considered leakage.

Figure 1.13: Affect of overlap in the extremes between it not protruding from the plunger and a 2 [mm] overlap between the plunger and core when the plunger is fully opened.

1.5 | Problem Statement

With the general tendency being wind turbines increase in capacity the mechanical transmission is being pushed to its limits. Alternative solutions are therefore, being investigated and with the hydraulic transmissions history of high power density it seems as if it would be a promising candidate to replace the mechanical transmission. However, inefficiencies at low displacement renders the current hydraulic transmissions infeasible and new technology is needed. Digital displacement technology could be this new technology needed. Further research is needed in this field to assess or achieve viability.

Current research revolves around Artemis who has multiple patents on the variable reluctance actuator, both in a directly actuated and a pilot configuration. Aalborg University's research primarily concerns the moving coil actuator which has both advantages and disadvantages. It has been shown that it has a superior transient response compared to the variable reluctance actuator and with its, roughly, travel distance independent force characteristic it can achieve a low pressure drop by increasing the travel distance.

Recently, the variable reluctance actuator has been researched at Aalborg University with a new geometry which has a lower moving mass, however, still suffering from the longer travel distance needed for a low pressure drop. This thesis will be a continuation of said project, seeking to partially counter the negative impact of a longer travel distance.

This has led to the following problem statement:

How can an electrically actuated fast switching variable reluctance valve be modelled and optimised for efficient digital hydraulic machines?

In order to resolve this problem statement a fast switching variable reluctance valve will be constructed and tested to verify the modelling methods used. The validity of one design will of course not validate all other valve designs completely, however, it will indicate whether or not the dominating factors are accounted for or if adjustments are needed in the modelling method.

Furthermore, the optimisation approach will be described and compared to other strategies. To ease the computational complexity a mimicking set of equations will be derived which characterises the same difficulties of the actual optimisation with relation to local solutions, variable dependence, and dominating variables, but not the specific problem at hand.

2 | Modelling

2.1 | Digital Displacement Machine

The DDM model can be divided into multiple submodels which will be explained in the following section with more emphasis on the electromagnetic and fluid dynamic characterisation of the valve. Furthermore, the interaction of each submodel will be explained to give an overview of the entire system.

The DDM model is divided into the following submodels and their interaction can be seen in Figure 2.1:

- Power Supply Unit (PSU): Supplies the electric power needed for the actuator to close.
- Electric model: The copper coil and the iron core of the valve make up a inductor-resistor (LR) circuit with position and current dependent inductance.
- Electromagnetic model: Finite element analysis characterising the actuator at different positions and currents.
- Mechanical model: The movement of the plunger depending on the net force exerted on it and its mass including.
- Orifice model: The flow through the valve as a function of the plunger position and pressure difference.
- Chamber dynamics: The pressure of the oil in the chamber depending on the change in chamber size and the net oil flow.

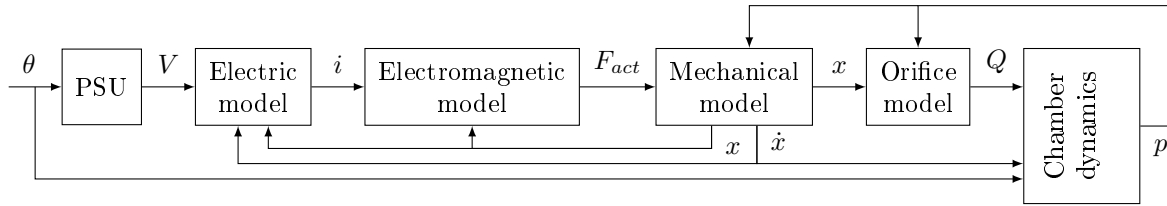


Figure 2.1: Model overview of how the different submodels interact.

2.1.1 | Power Supply Unit

The PSU is assumed ideal with a voltage range of ± 48 [V] and a current range of ± 20 [A]. It has no switching frequency or resolution limitations, no electric switching losses, and no internal resistance. This is assumed since the bandwidth of a typical PSU is much greater than that of the electric circuit of the valve since it has a high inductance and low resistance which gives a slow electrical response. As an example the prototype with 300 turns has a current build up from 0 [A] to 20 [A] in approximately 14 [ms] or 70 [Hz] which is much slower than that of a typical PSU.

A simple high gain P-controller is used to control the voltage across the coil so that the wanted current is obtained. When the valve is sought to be actively closing the current reference is set to the maximum current and at all other times the current is sought to be zero. It is noted that this is a rather simple or perhaps even

crude way of controlling the valve compared to more advanced control methods which use e.g. using a boost voltage in the beginning to quickly obtain a high current when wanted, however, this would require special power electronics and go against the spirit of keeping things simple.

2.1.2 | Electric Model

The actuator is modelled as a simple LR circuit in series where the inductance depends on the plunger position and coil current. The voltage equation for such a circuit can be expanded using the chain and product rules yielding

$$v = Ri + \frac{dLi}{dt} = Ri + L \frac{\partial i}{\partial t} + i \frac{\partial L}{\partial x} \frac{\partial x}{\partial t}. \quad (2.1)$$

By solving for the current gradient, and using the dot notation to indicate the derivative with respect to time, the following expression is obtained

$$\dot{i} = \frac{1}{L} \int v - Ri - i \frac{\partial L}{\partial x} \dot{x} dt. \quad (2.2)$$

This is a relatively simple expression consisting of constants and time dependent variables, except for the inductance and its spatial derivative. These are not simple algebraic expressions and are found using Finite Element Analysis as explained in Section 2.2.

2.1.3 | Electromagnetic model

When current is flowing through a wire, a magnetic field is induced in around the coil as seen in Ampère's law given by

$$\nabla \times B = \mu \left(J + \epsilon \frac{\partial H}{\partial t} \right). \quad (2.3)$$

The strength of this magnetic field depends on the reluctance around the coil, the current through the coil and the number of turns of the coil. Since the valve topology of interest is the solenoid it operates using the principle of position dependent reluctance. That is, if a flux is flowing through a free part, which by changing its position, will change the reluctance of the magnetic circuit, a force will be exerted on this part and accelerate it towards the position in which the reluctance is minimised. For the valve proposed, this means that when the coil is excited a force will be exerted onto the plunger and close the valve.

The electromagnetic modelling has been elaborated in Section 2.2.

2.1.4 | Mechanical Model

The mechanical model describes the plungers position, velocity, and acceleration, which is affected by the different forces such as actuator-, spring-, fluid-, and movement induced force. The acceleration is derived from Newton's second law of motion stating that the acceleration is equal to the sum of all forces divided by the accelerating mass. It is noted that the accelerating mass consist of both the iron plunger and the mass of the oil in its immediate surrounding.

Expressing the mass of the plunger is a simple matter of obtaining the volume and the multiplying it by the density of iron. The mass of the surrounding oil, however, is more difficult since a transient Computational Fluid Dynamics (CFD) analysis has to be conducted for a precise approximation, and strictly algebraic approximations are often poor and insufficient for complex geometries. However, the plunger at hand has a relatively simple design and can be approximated by a 2D plate due to its axisymmetry. The added mass is further studied in Section 2.3.5.

The forces affecting the plunger, which can be seen in Figure 2.2, are described by

- **Actuator force:** The force generated by the coil in the closing direction.
- **Spring force:** The force exerted by the spring in the opening direction to keep the valve open when the fluid flow would otherwise close it.
- **Flow force:** The force exerted by the fluid moving past the plunger due to the pressure drop.
- **Movement induced force:** The force acting exerted by the fluid on the plunger as it is moving.

Some forces are, however, not modelled due to their complexity and lack of importance, e.g. the end damping as the plunger is closing and just about to make contact with the core the oil in-between the plunger and core must be squeezed out which is both complex to calculate and only affects the plunger for a very small period.

Actuator force The actuator force, dependent on both the current and plunger position, is investigated in Section 2.2.

Spring force The spring force depend on the plunger position and is defined by

$$F_s = F_{s,init} + K_s(x_{max} - x) \quad (2.4)$$

where $F_{s,init}$ is the force of the spring as the plunger is in its outermost position ($x = x_{max}$) and K_s is the spring stiffness.

Flow force As the fluid moves past the plunger there is a loss of energy to heat in the form of a pressure drop. This pressure drop means that there is a greater pressure on the inlet side of the plunger than on the outlet side of the plunger. This pressure drop is simulated in the plunger's outermost position and can then be expressed as a function of the plunger position and volumetric flow.

Like the pressure drop, as examined in Sections 2.3.2-2.3.3, the fluid force can be expressed by

$$F_f = \left(\frac{x_{max}}{x}\right)^\varphi (K_{f1}Q + K_{f2}|Q|Q) \quad (2.5)$$

where K_{f1} , K_{f2} are geometry dependent positive coefficients found using Computational Fluid Dynamic (CFD) modelling.

Movement induced force The movement induced forces comprise of two different forces related to the velocity of the plunger. These forces are the viscous force which is proportional to the velocity and the drag for which is proportional to the sign dependent velocity squared yielding the following expression

$$F_m = K_v\dot{x} + K_d|\dot{x}|\dot{x}, \quad (2.6)$$

where K_v is the viscous coefficient and K_d is the drag coefficient which are further described in Section 2.3.4.

2.1.5 | Orifice Model

The orifice model expresses the relationship between the volumetric flow, the pressure drop from inlet to outlet, and the plunger position when the valve is open. This is done using the expression

$$\Delta p = \left(\frac{x_{max}}{x}\right)^\delta (K_1Q + K_2|Q|Q), \quad (2.7)$$

where K_1 and K_2 are geometry specific positive coefficients found using CFD. The term $\left(\frac{x_{max}}{x}\right)^\delta$ adjusts the increase in pressure drop as the valve is closing. This equation can be rearranged so that the flow is expressed in terms of the plunger position and pressure difference.

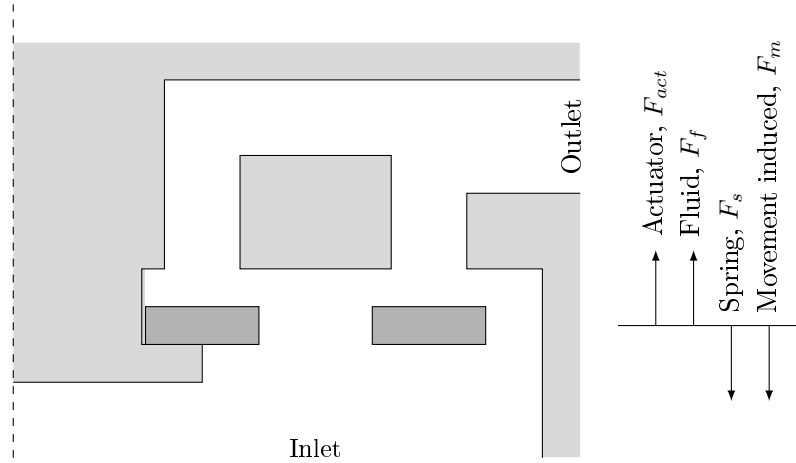


Figure 2.2: Forces affecting the plunger and their respective direction when positive.

2.1.6 | Chamber Dynamics

The chamber is modelled using the continuity equation for a fluid with constant density which is given by

$$\dot{p} = \frac{\beta}{V_c} \left(Q_{in} - Q_{out} - \dot{V}_c + A_s \dot{x}_L - A_s \dot{x}_H \right) \quad (2.8)$$

where \dot{p} is the gradient of the chamber pressure, β is the oil stiffness, V_c is the chamber volume, Q_{in} is the flow into the chamber which is defined as the flow through the HPV, Q_{out} is the flow out of the chamber which is defined as the flow through the LPV, \dot{V}_c is the change in chamber size due to the piston movement, and the two last terms are the changes in chamber size due to the movement of the two plungers which are significant for fast switching valves due to the high plunger velocity.

The oil stiffness is modelled using the IFAS model given by [5]

$$\beta = \frac{(1 - \alpha) \left(1 + \frac{m(p-p_0)}{\beta_0} \right)^{\frac{-1}{m}} + \alpha \left(\frac{p_0}{p} \right)^{\frac{1}{\kappa}}}{\frac{1-\alpha}{\beta_0} \left(1 + \frac{m(p-p_0)}{\beta_0} \right)^{\frac{-(m+1)}{m}} + \frac{\alpha}{\kappa p_0} \left(\frac{p_0}{p} \right)^{\frac{\kappa+1}{\kappa}}} \quad (2.9)$$

where α [%] is the air to oil ratio, $m = 11.4$ is the stiffness pressure gradient, $p_0 = 1$ [bar] is the reference pressure, $\beta_0 = 15500$ [bar] is the reference stiffness, and $\kappa = 1.4$ is the adiabatic constant of air. This expression has been plotted in Figure 2.3. Although the article only measures the effective bulk modulus at low pressures, up to 80 [bar], it closely approaches a straight line at this pressure and therefore extrapolation is considered to be a fair approximation. For this model the air to oil ratio is defined as 0.5 [%].

The chamber volume is expressed by

$$V_c = V_d + A_p x_p \quad (2.10)$$

where V_d is the dead volume, which is defined as the chamber volume when it is at a minimum at TDC, A_p is the wet area of the piston head, and x_p is the piston position which is zero when the piston is at the TDC. It is noted that, though the plunger velocity is significant when describing the chamber volume derivative, the plunger position is not significant when describing the chamber volume and is therefore neglected.

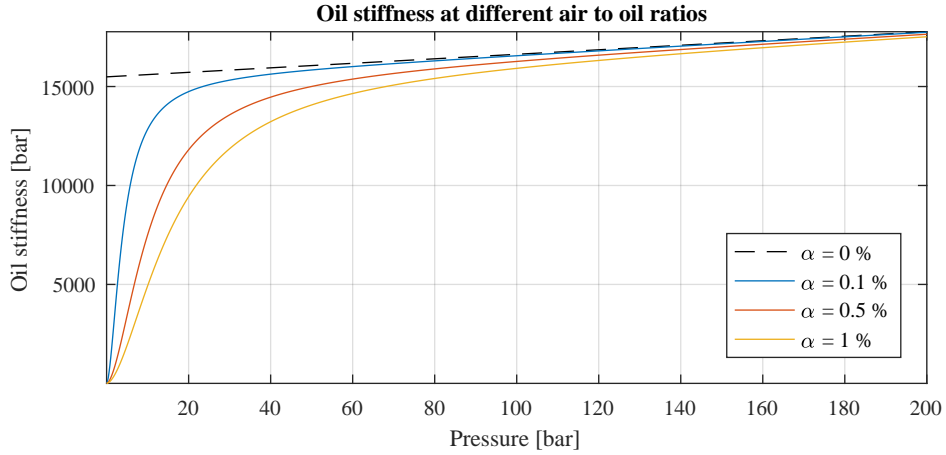


Figure 2.3: Bulk modulus as a function of the pressure and for different air to oil ratios.

2.2 | Electro Magnetic Modelling

The valve is modelled electromagnetically using a selection of Maxwell's four equations which describe the interaction between electricity and magnetism. These are all given in the following table. It is noted that the nabla operator is to represent the divergence ($\nabla \cdot$) and curl ($\nabla \times$) of the field.

Name	Differential form	Description
Gauss's Law	$\nabla \cdot \underline{H} = \frac{\rho}{\epsilon_0}$	The electric field diverging from a closed system is equal to the charge density over the permittivity of free space.
Gauss's Magnetism Law	$\nabla \cdot \underline{B} = 0$	The magnetic flux diverging from a closed system is equal to zero, meaning there exist not magnetic monopoles, i.e. magnets always come in north- and south pole pairs.
Faraday's Law	$\nabla \times \underline{H} = -\frac{\partial \underline{B}}{\partial t}$	The electric field generated about a point is proportional to the time rate of change of the magnetic field.
Ampère's Law with Maxwell's addition	$\nabla \times \underline{B} = \mu_0 \left(\underline{J} + \epsilon_0 \frac{\partial \underline{H}}{\partial t} \right)$	The magnetic field induced around a conductor is described by the current density and the time rate of change of the electric field.

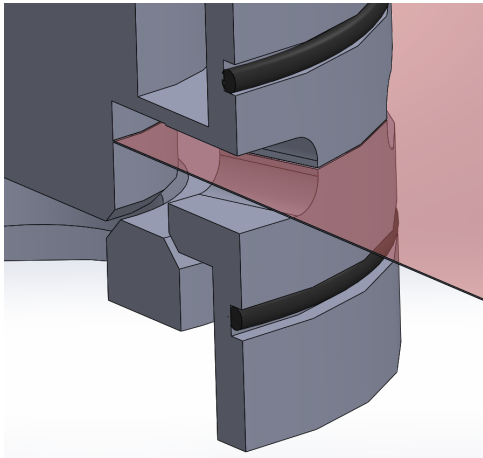
For static simulations of the magnetic flux in a system only Gauss's magnetism law and Ampères without the time derivative is needed. This means that software such as FEMM, which is a finite element software, solves the differential equations for each node given by

$$\nabla \cdot \underline{B} = 0 \text{ and } \nabla \times \underline{B} = \mu_0 \underline{J}.$$

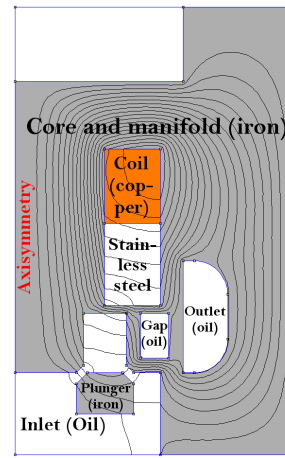
This yields the magnetic flux at each node from which the actuator force, inductance, and inductance gradient can be obtained. It is noted that since the simulation accuracy depends on the mesh resolution it has been studied in Appendix A.3.

The geometry is almost axisymmetric, however, not entirely. One of the aspects which are not entirely axisymmetric is the port between the chamber above the plunger and the outlet to the manifold which can be seen in Figure 2.4. To compensate for the lack of magnetically conductive iron a rectangle with the material characteristics of oil is inserted into the iron flux path outline as seen in Figure 2.4. This rectangle is scaled so that the ratio between iron and oil is conserved for the ring.

Simulating this geometry at various positions and magnetomotive forces will yield a map of the actuator force and inductance. For the example geometry shown in Figure 2.4 the force as a function of position and magnetomotive

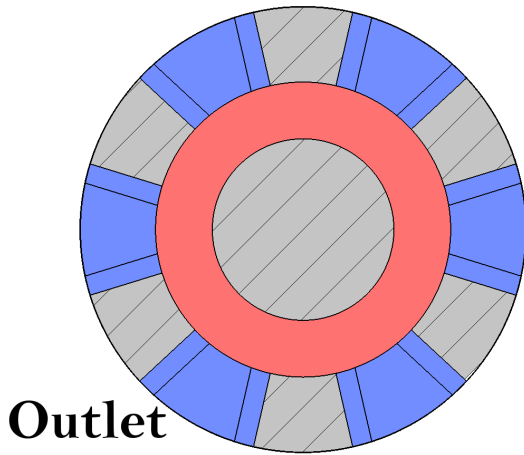


(a) Outlet showing its lack of axisymmetry.

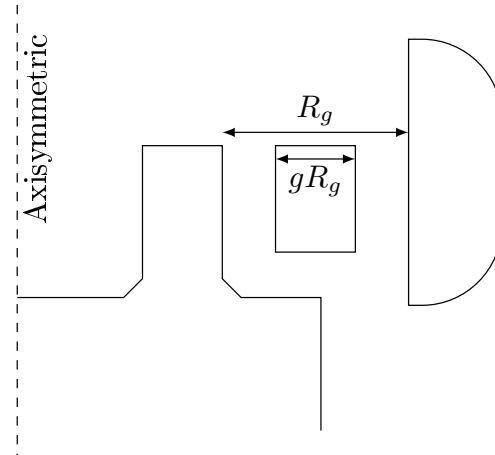


(b) Compensating, for the lack of axisymmetry, by inserting the *Gap (oil)* rectangle.

Figure 2.4: Axisymmetry compensation at the outlet.



(a) Cross sectional view of the actuator as seen normal to the red tinted plane in 2.4a. The scaling factor g is the ratio between the outlet area (blue) and the total ring (blue and grey).



(b) Gap ratio as defined in FEMM.

Figure 2.5: Appropriate scaling of the gap rectangle for electromagnetic modelling.

force can be seen Figure 2.6. From these figures it can be seen that as the plunger is closing the actuator force increases due to the now smaller oil gap between core and plunger. For the magnetomotive force characteristic it can be seen that the force increases rapidly at smaller magnetomotive forces and as it reaches approximately 1000 [A] its slope falls due to the iron between the coil and the axisymmetric line saturating meaning its permeability is lowered. The permeability can be seen as the magnetic field strength dependent gradient of the BH curve shown in Figure 2.8.

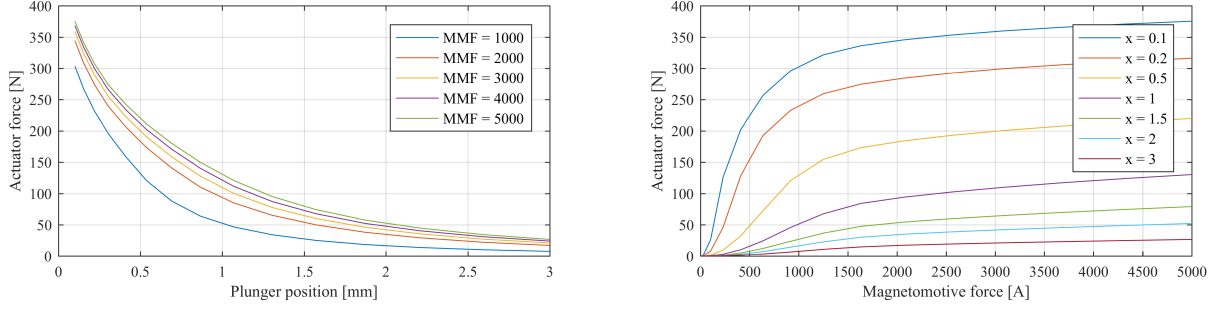


Figure 2.6: Actuator force mapped at various positions and currents.

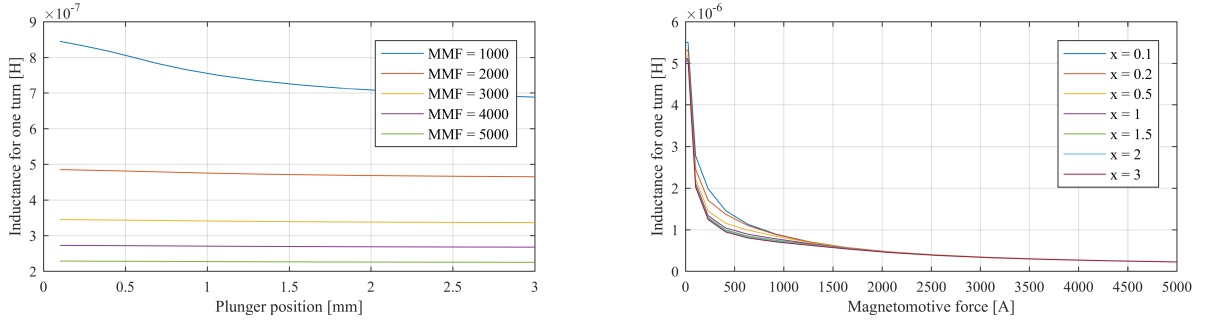


Figure 2.7: Inductance mapped at various positions and currents.

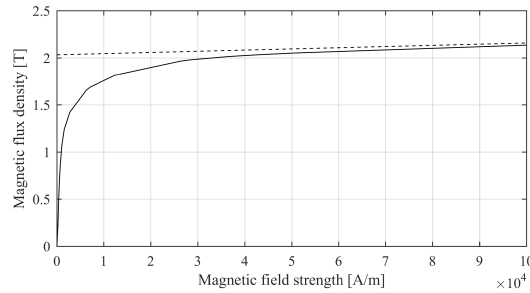


Figure 2.8: BH curve of iron. The dashed line is its asymptote with a slope of $\mu_0 = 4\pi \times 10^{-7} \text{ [N A}^{-2}\text{]}$.

2.2.1 | Time Dependent Force Characteristic

The above analysis is only valid for the static case, that is, there is no change in magnetomotive force and no change in plunger position. This section will focus on the transient characteristics and its effect on the behaviour of the valve.

Since the iron core is also electrically conductive the change in flux will introduce a current orthogonal to the direction of the flux. These currents are known as eddy currents. In Figure 2.9 the effect of these eddy currents can be seen where a current step in the coil is induced and the flux starting immediately around the coil and then propagating throughout the core. Video of this is available at <https://youtu.be/E7M2jB-eRp4>. As can

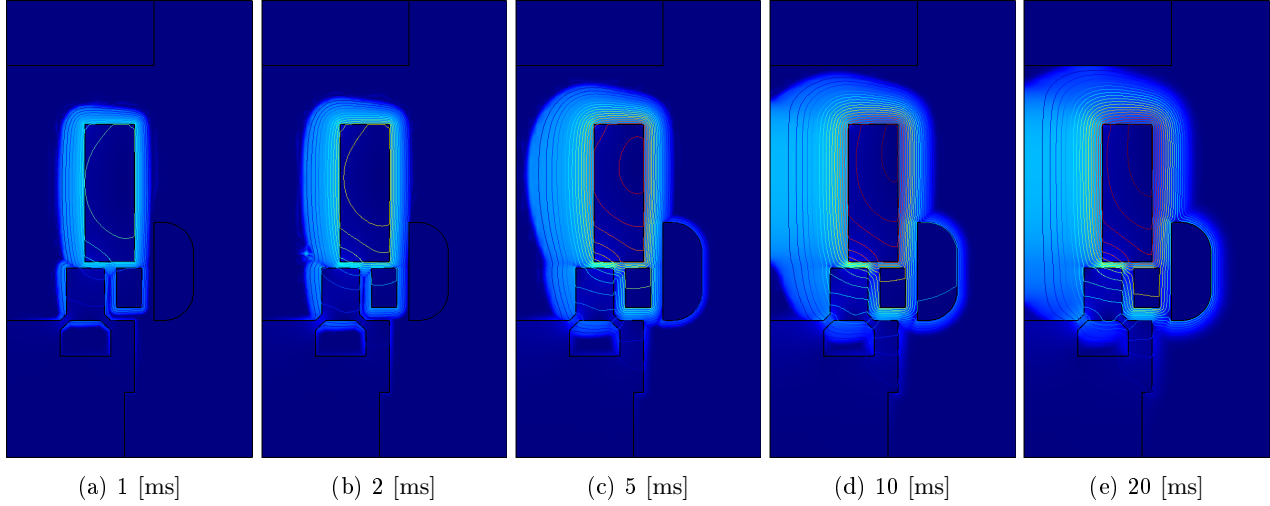


Figure 2.9: Transient model when subject to current step. Simulation can be seen at <https://youtu.be/E7M2jB-eRp4>.

be seen in Figure 2.9a there is virtually no flux going through the plunger and therefore it is expected to see no significant actuator force at this time. This can further be seen in Figure 2.10 where the actuator force as a function of time is shown for the cork test population. It can be seen that 90 % of the steady state force is achieved between 3.5 [ms] and 7.5 [ms]. It is further seen that these step responses can be closely resembled by a second order transfer function. A conservative approximation is to construct a transfer function reaching 90 % in 8 [ms], making it slower than the slowest test design. This approximation can be seen as the dashed line in Figure 2.10 and is given by

$$G_{eddy} = \frac{F}{i} = K \frac{\omega_n^2}{s^2 + 2\zeta\omega_n s + \omega_n^2}, \quad \omega_n = 430 \text{ [rad/s]}, \quad \zeta = 0.9 \quad (2.11)$$

where K is the relation between the steady state actuator force and current.

2.3 | Fluid Mechanic

The valve is modelled and simulated fluid dynamically in order to approximate the pressure drop across the valve and the fluid force affecting the plunger. This is done in a 2D axisymmetric finite volume simulation in COMSOL since most of the geometry is axisymmetric.

It is modelled stationary using the Navier-Stokes equation for laminar flow where the fluid is incompressible, no turbulence modelling, and with no external force or gravity yielding the following expressions in differential form

$$\underbrace{\rho(\mathbf{u} \cdot \nabla)\mathbf{u}}^{(1)} = \underbrace{-\nabla p}_{(2)} + \underbrace{\nabla \cdot \left(\mu \left(\nabla \mathbf{u} + (\nabla \mathbf{u})^T \right) \right)}_{(3)}, \quad \underbrace{\rho \nabla \cdot \mathbf{u}}_{(4)} = 0 \quad (2.12)$$

where ρ is the density of the fluid, \mathbf{u} is the velocity of the fluid, p is the pressure of the fluid, μ is the viscosity of the fluid, and ∇ is the nabla or del operator which is a convenient way of notating the gradient and divergence

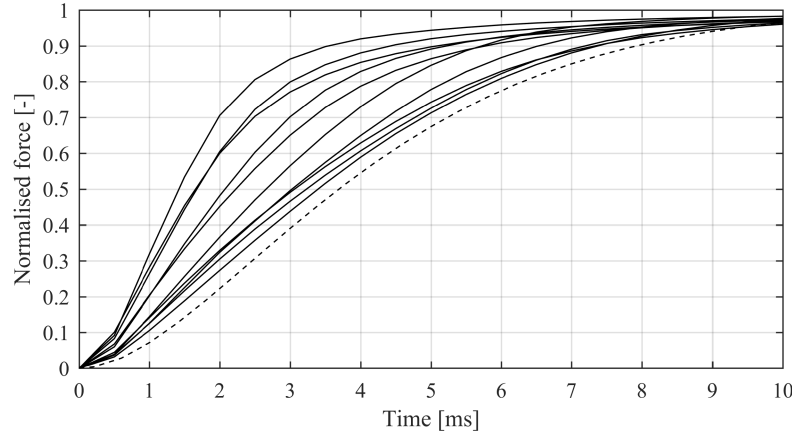


Figure 2.10: Normalised force as a function of time with current step from 0 [A] to 20 [A] for the cork test population in Appendix B as well as the conservative approximation G_{eddy} .

of, for instance, the velocity field \mathbf{u} by $\nabla \mathbf{u}$ and $\nabla \cdot \mathbf{u}$, respectively. The different terms express the fluids inertial force (1), the pressure force (2), the viscous or shear force of the fluid (3), and the continuity equation for constant fluid density (4).

It is noted that one has to be cautious when using the nabla operator since commutativity is invalid, i.e. $(\nabla \cdot \underline{a}) \underline{b} \neq (\underline{a} \cdot \nabla) \underline{b}$. This can be further seen since these two terms can be rewritten for three dimensions as

$$\begin{aligned} (\nabla \cdot \underline{a}) \underline{b} &= \left(\frac{\partial a_x}{\partial x} + \frac{\partial a_y}{\partial y} + \frac{\partial a_z}{\partial z} \right) \underline{b} = \frac{\partial a_x}{\partial x} \underline{b} + \frac{\partial a_y}{\partial y} \underline{b} + \frac{\partial a_z}{\partial z} \underline{b} \\ (\underline{a} \cdot \nabla) \underline{b} &= \left(a_x \frac{\partial}{\partial x} + a_y \frac{\partial}{\partial y} + a_z \frac{\partial}{\partial z} \right) \underline{b} = a_x \frac{\partial \underline{b}}{\partial x} + a_y \frac{\partial \underline{b}}{\partial y} + a_z \frac{\partial \underline{b}}{\partial z} \end{aligned}$$

To simulate the fluid some boundary conditions are needed. For simulating the valve the inlet is set to a volumetric flow, the outlet is set to zero pressure to better visualize the pressure drop, and the fluid velocity at the wall is set to zero due to the no slip condition.

COMSOL uses the discrete form of eq. 2.12 to solve for the pressure and velocity of all cells in the mesh using the finite volume method. Since it is known that the correctness of the solution depends on the resolution of the mesh, as is the case with FEA, the test population will be studied under different mesh resolutions in Appendix A.3 with respect to the flow forces affecting the plunger and the pressure drop from inlet to outlet.

2.3.1 | Oil Temperature

Since the viscosity, that is a fluids resistance to flow (water has a low viscosity, while honey has a high viscosity), depends on the temperature of the oil. Since the oil is more viscous when it is cold the pressure drop and fluid force are expected to be higher. The dynamic viscosity of engine oil below 80 [°C] is defined COMSOL as

$$\begin{aligned} \mu_{oil} = & 4.26693 \times 10^4 - 7.41172 \times 10^2 \cdot T^1 + 5.36052 \cdot T^2 - 2.066034 \times 10^{-2} \cdot T^3 + \dots \\ & 4.47492 \times 10^{-5} \cdot T^4 - 5.16405 \times 10^{-8} \cdot T^5 + 2.480338 \times 10^{-11} \cdot T^6 \end{aligned} \quad (2.13)$$

where T is the oil temperature in Kelvin. The expression can be seen in Figure 2.11. The pressure drop and flow force at different oil temperatures can be seen in Figure 2.12 where, as expected, the pressure drop is significantly higher at the lower oil temperature. Henceforth, the temperature is defined as 40 [°C] since this is a reasonable minimum operating temperature of the test stand at Aalborg University. The oil in said test stand is typically kept around this temperature with it increasing during operation to about 55 [°C].

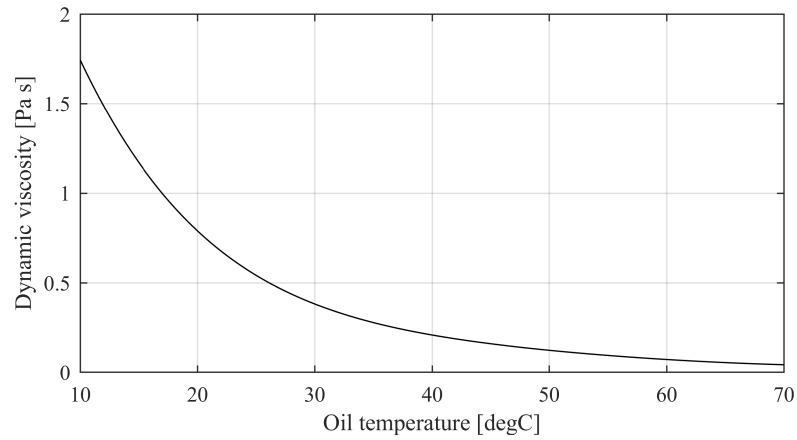


Figure 2.11: Dynamic viscosity of engine oil as defined in COMSOL.

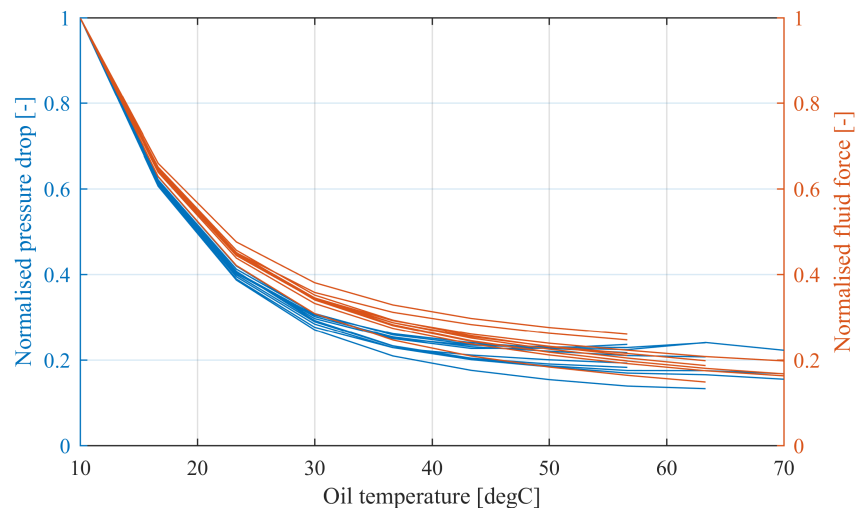


Figure 2.12: Normalised pressure drop and flow force for the cork test population dependent on oil temperature.

2.3.2 | Flow Dependence

For a specific design the pressure drop across the valve depends on both the plunger position and volumetric flow. From the orifice equation given by

$$Q = C_d A_d \sqrt{\frac{2}{\rho} |\Delta p|} \text{sign}(\Delta p) \quad (2.14)$$

which would indicate that the pressure drop is proportional to the flow squared. However, the orifice equation is derived from a turbulent case with sharp orifice edges. Therefore, the pressure drop is investigated for this case. As can be seen in Figure 2.13 the pressure drop and flow force can be accurately approximated by a quadratic equation. The quadratic approximation for the pressure drop of a fully opened valve is given by

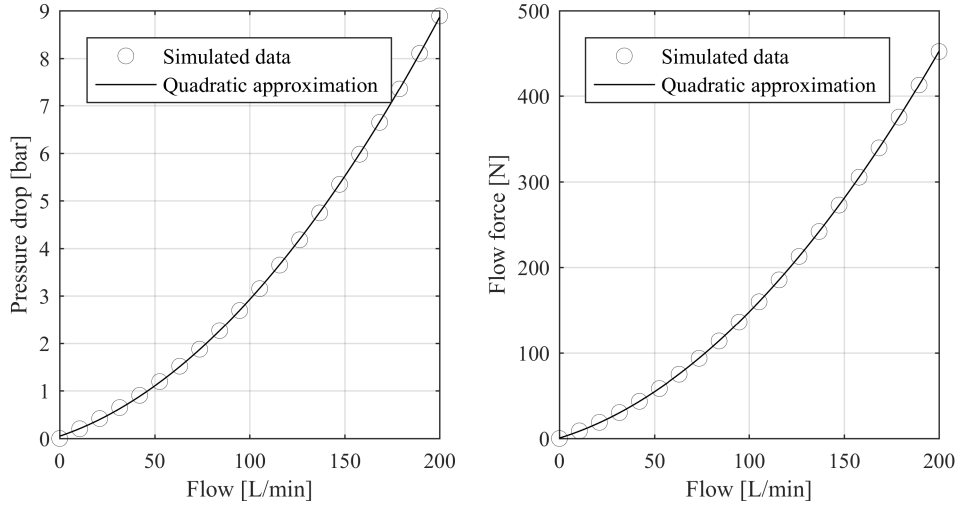


Figure 2.13: Flow characteristic dependent on the plunger position of a single design.

$$\Delta p = K_{\Delta p,1} Q + K_{\Delta p,1} Q |Q|, \quad (2.15)$$

which when evaluated at two points, $(Q_1, \Delta p_1)$ and $(Q_2, \Delta p_2)$, can be rearranged to solved for the coefficients given by

$$K_{\Delta p,1} = \frac{\Delta p_1 Q_2^2 - \Delta p_2 Q_1^2}{Q_1 Q_2 (Q_2 - Q_1)} \quad \text{and} \quad K_{\Delta p,2} = \frac{\Delta p_1 Q_2 - \Delta p_2 Q_1}{Q_1 Q_2 (Q_1 - Q_2)} \quad (2.16)$$

and likewise for the flow force.

2.3.3 | Position dependence

Since the pressure drop and flow force increases as the plunger is closing the term correcting for this could be the inverse relative plunger position to the power of some exponent as described by

$$\Delta p = \left(\frac{x_{max}}{x} \right)^\delta (K_{\Delta p,1} Q + K_{\Delta p,2} Q |Q|) \quad \text{and} \quad F_f = \left(\frac{x_{max}}{x} \right)^\varphi (K_{f,1} Q + K_{f,2} Q |Q|).$$

Since the variable x is in the denominator this causes a division by zero when the valve is the fraction grow to a very high number when it approaches zero. To avoid this the maximum value of the fraction is set at 100. Although this is not physically true it is considered reasonable due to the small time between the valve being 99 % closed and being totally closed.

By keeping the flow constant at $24 \text{ [l min}^{-1}\text{]}$, that is 20 % of the maximum flow and a reasonable estimate of the flow when the valve has to close, the term can be studied. By rearranging the two flow characterising equations and normalising at the outermost plunger position the following expressions are obtained

$$\frac{\Delta p(x) / \Delta p(x_{max})}{\left(\frac{x_{max}}{x}\right)^\delta} \quad \text{and} \quad \frac{F_f(x) / F_f(x_{max})}{\left(\frac{x_{max}}{x}\right)^\varphi},$$

which, if characterised ideally, should equal one. However, the complex nature of fluid dynamics rarely yields ideal approximations and therefore different exponents are tried for the ten cork test designs. These approximations can be seen in Figures 2.14 and 2.15 for the pressure drop and flow force, respectively.

As can be seen the best fitting exponent is between two and three. Upon further investigation of the ten cork designs the exponent was tuned to 2.4 for the pressure drop and 2.7 for the flow force as seen in Figure 2.16.

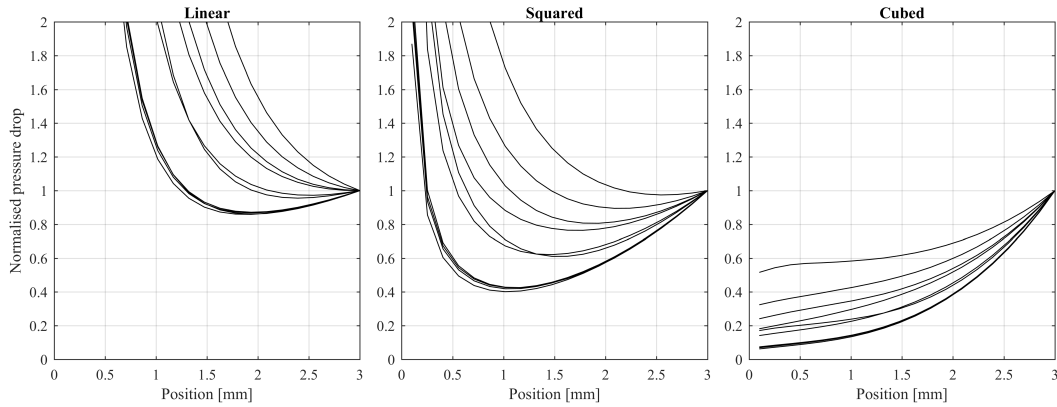


Figure 2.14: Normalised pressure drop dependent on plunger position with varying exponent.

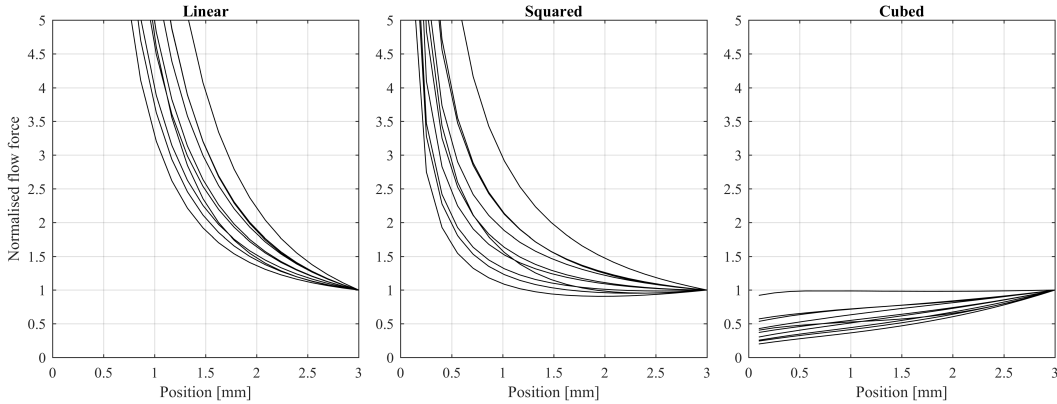


Figure 2.15: Normalised flow force dependent on plunger position with varying exponent.

2.3.4 | Movement induced forces

The movement induced force are, as previously mentioned, the viscous force and drag force. Due to the relatively small contact area between parts while the plunger is moving this force is neglected. The drag force is approximated using the drag equation given by

$$F_d = \frac{1}{2} C_d A \rho |\dot{x}| \dot{x} = K_d |\dot{x}| \dot{x}, \quad (2.17)$$

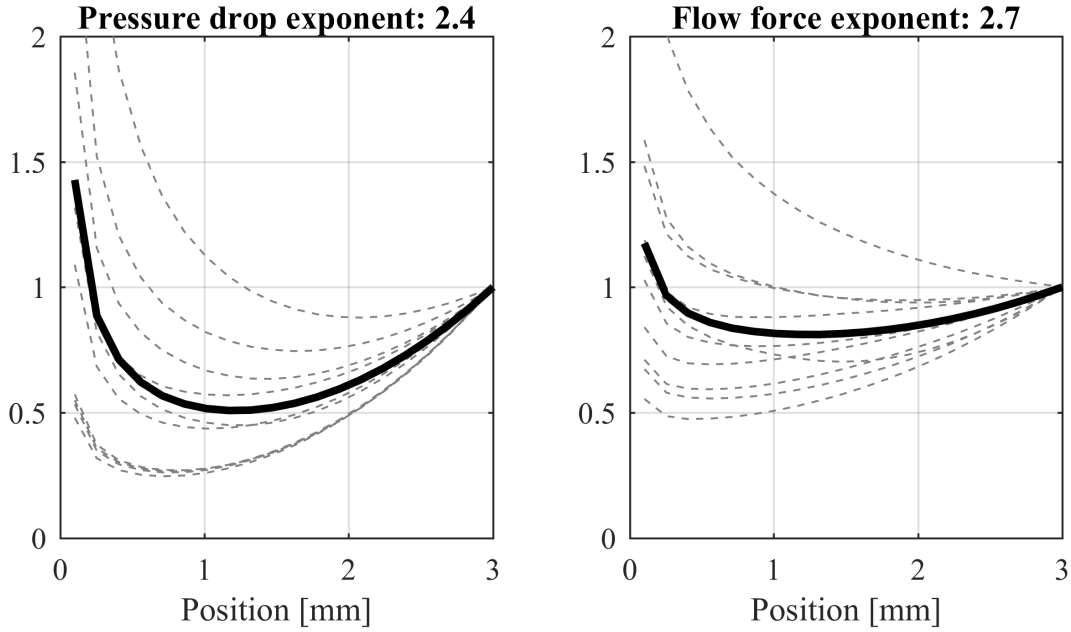


Figure 2.16: Normalised pressure drop and fluid force at different positions with position exponents of $\delta = 2.4$ and $\varphi = 2.7$. The thick line is the mean of the ten designs at the given position.

where C_d is the drag coefficient where a 2D plate is chosen due to the 2D axisymmetric shape of the plunger and defined as 1.9 [3, p. 599], A is the shadow area of the plunger, and ρ is the density of oil.

2.3.5 | Added mass

As described in [13] the added mass of a 2D plate can be described by

$$m_a = \rho \pi a^2 \quad (2.18)$$

where a is the distance from the centre of the plate to the edge. By revolving this added mass about the valves axisymmetry the added mass is described by

$$m_a = (2\pi r) \rho \pi a^2 \quad (2.19)$$

where r is the distance from the centreline to the middle of the plate and can be seen in Figure 2.17. For

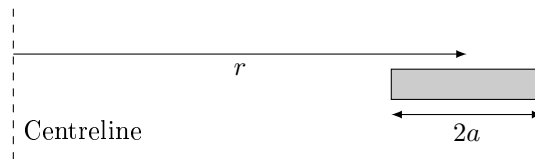


Figure 2.17: Variables for calculating the added mass of a ring.

reference a typical plunger could be given by $r = 14$ [mm], $a = 3$ [mm] giving it a moving mass of 2.2 [gram] which is relatively much compared to the mass of the plunger typically ranging between 10-20 [gram].

2.4 | Mechanical Stress Considerations

With the high pressure that the valve operates under an enormous amount of force is applied to the valve. Due to the limits of this study the investigation of these forces are severally limited and therefore only a few areas of interest are investigated leaving others, or perhaps a complete study of the valve, open for further work.

The areas investigated are

- Stress on the upper region.
- Stress on the lower wall region.
- Stress on the resting surface.

The first two will be studied using FEA in Comsol and can be see in Figures 2.18-2.19, while the third will be studied analytically.

The upper region was found to be highly sensitive to the distance between the O-ring pocket and the outside of the coil pocket. Lowering the O-ring pocket would be ideal, however, its placement is fixed due to the design of the manifold at hand. This leaves the lower right-hand corner to be moved either up or left which both of which will cause the available coil area to shrink in size and therefore is undesirable. Through trial and error the a sufficient distance between theses two corners was found to be approximately 2 [mm] radially and 2 [mm] axially. It is noted that the analysis, even at these distances, showed a high local stress in the corner of the coil (450 MPa) as can be seen in Figure The lower region is less difficult to design and by trial and error it was

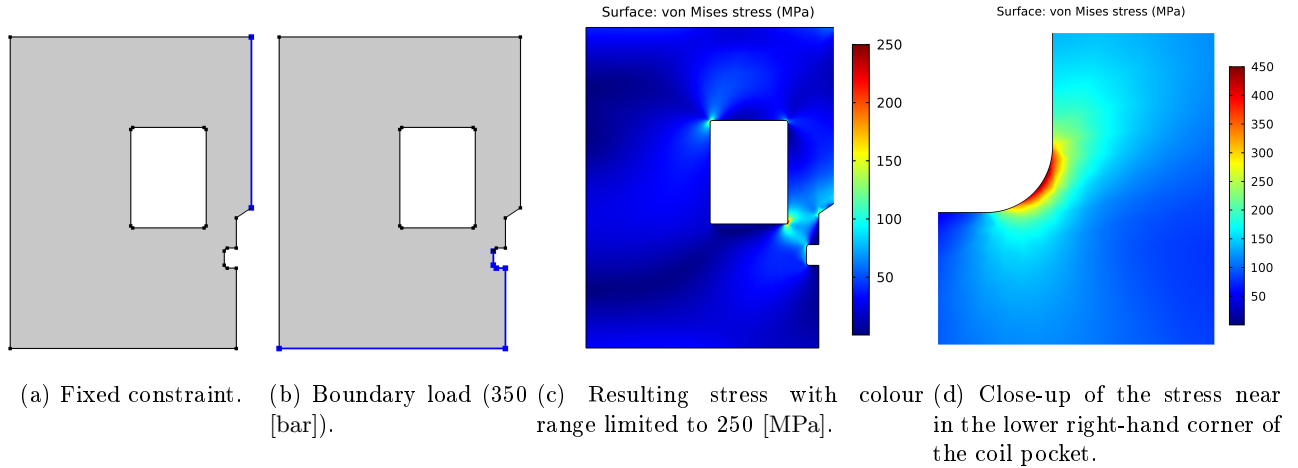


Figure 2.18: Structural stress studies investigated for the upper region.

found that a wall thickness of 2 [mm], however, a 3 [mm] wall thickness was chosen to add some safety factor. The third area of interest is the resting surface, that is, the surface of the core which the plunger rests on the valve is closed. If this area gets too small it cannot provide a sufficient equal and opposite reacting force to act against the force exerted by the high pressure on the bottom side of the plunger as seen in Figure 2.20. This will cause the material to deform by leaving marks, or at worst cause the material to buckle or break.

The projected area and pressure area when revolved around the axisymmetric axis is given by

$$A_{rest} = \pi \left((v_1^2 - (v_1 - g_1)^2) + (v_1 + v_2 + g_2)^2 - (v_1 + v_2)^2 \right) \quad (2.20)$$

$$A_{pressure} = \pi \left((v_1 + v_2 + g_2)^2 - (v_1 - g_1)^2 \right). \quad (2.21)$$

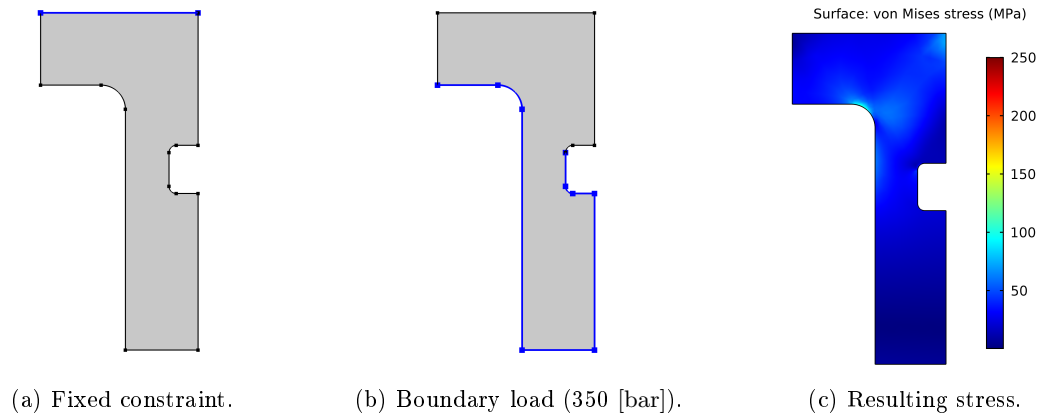


Figure 2.19: Structural stress studies investigated for the lower region wall.

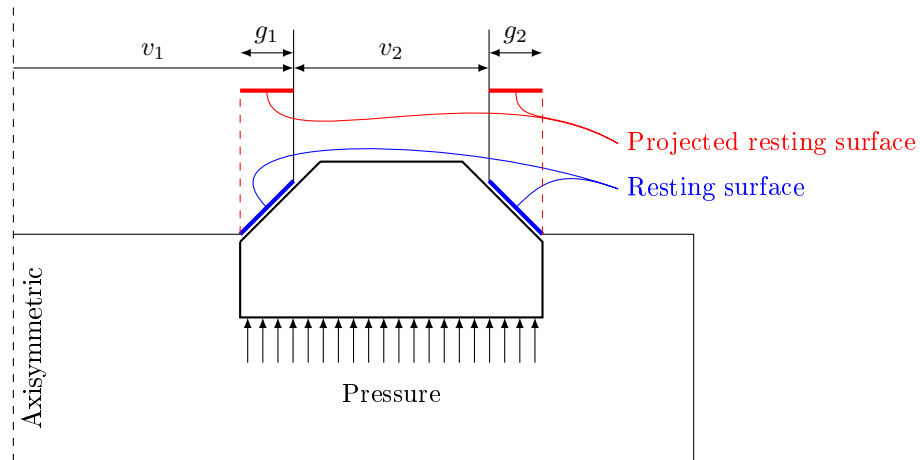


Figure 2.20: Resting surface and the projected resting surface in the axial direction, which will provide the reacting force to the one exerted by the plunger.

CHAPTER 2. MODELLING

The stress on the resting surface is then given by

$$\sigma = p \frac{A_{pressure}}{A_{rest}} \quad (2.22)$$

which for an example case where $v_1 = 9$ [mm], $v_2 = 6$ [mm], $g_1 = 1$ [mm], $g_2 = 1$ [mm], and a pressure of 350 [bar] yields a stress on the resting surface of 140 [MPa] which is well within the yield strength typically associated with steel.

3 | Optimisation

The overall objective of the DDM is to compete with traditional large scale transmission solutions. For this to be the case it must be efficient, reliable, and cheap. The two latter are difficult to quantify when only looking at a single valve, however, with the simple geometry proposed that is made up of off-the-shelf materials these are considered non issues and out of the scope of this thesis. Left is the efficiency is sought optimised in this chapter.

As seen in Figure 1.4 the efficiency of the machine is related to the pressure drop and switching time. Furthermore, a valve with a high electrical power consumption will negate the efficiency gained from the two first objectives and require a more powerful power supply. The objectives of the optimisation must therefore reflect these three concerns.

3.1 | Object Functions

The objectives to minimise have been separated into three different object functions.

- Pressure drop: The energy lost due to the pressure drop when the valve is open.
- Fluid power loss while switching: The energy lost when the valve is switching from open to closed.
- Electric power consumption: The power delivered by the power supply.

These functions will be discussed in the following sections.

3.1.1 | Pressure drop

Finding the pressure drop across each valve is relatively simple. The outlet pressure is defined as 0 [bar], the inlet flow is defined as $120 \text{ [lmin}^{-1}\text{]}$, and the average inlet pressure is defined as the pressure drop. Due to the nonlinearity of the pressure drop as function of flow the objective is defined by the integral of the fluid power loss during a single revolution given by

$$\text{Pressure drop: } O_1 = \int_0^{T_{rev}} \Delta p(Q)Q(t)dt \quad (3.1)$$

3.1.2 | Fluid power loss while switching

To asses the fluid power loss associated with switching, one must first define what switching time is and which flow is reasonable during the switch.

There are multiple ways of defining the switching time, depending on the application and interest, some of which are listed below

1. The total time where a current is going through the coil.

2. The time from where a positive voltage is applied to the coil until the plunger starts to close.
3. The time from where a positive voltage is applied to increase the current of the coil to when a negative voltage is applied to decrease the current of the coil.
4. The time from where a positive voltage is applied to the coil until the valve is closed.
5. The time from where the plunger starts to move until the valve is closed.

Since the electrical losses are considered negligible compared to the fluid losses the fifth case is chosen as the definition of the switching time. It is noted that this choice is contradicting with the definition used in [9] which uses the fourth definition, however, it is noted that the valve studied in there is a moving coil valve which typically has a much faster electric and force response than the solenoid which typically has many turns, thereby increasing inductance. Therefore, the distinction between the fourth and fifth definition is more important for the solenoid valve.

However, not considering the electrical rise time has its disadvantages in that one must add an appropriate safety margin for when to apply voltage to the coil to compensate for the relative uncertainty associated with the rise time, i.e. it is easier to control the closing angle if the rise time, of the electrical circuit, is 1 [ms] than if it is 10 [ms]. This issue is considered solvable through experimentation where a precise rise time can be found.

The valve closing will be modelled dynamically with the forces acting on the plunger being the actuator, spring, and fluid force. It is noted that, for the sake of simplicity, movement induced forces are neglected.

Firstly, the fluid force at the ideal closing angle for an infinitely fast switching valve is investigated by modelling the closed chamber. The pressure of the closed chamber is given by

$$p = \int_{\theta_{DC}-\theta_c}^{\theta_{DC}} \frac{\beta(p) \dot{V}(\theta)}{V(\theta)} d\theta + p_0, \quad (3.2)$$

where θ_{DC} is the machine angle at the dead centre of interest, θ_c is the wanted closing angle, and p_0 is the initial chamber pressure. It is noted that this method does not leave any time for the valves to open and close, however, is considered a good conservative assumption since closing the valve sooner would cause the fluid force to be stronger and therefore decrease closing time.

The necessary closing angle is shown in Figure 3.1. When going from low pressure to high pressure chamber must be closed for 13.3 [deg] and when going from high pressure to low pressure it must be closed for 21.3 [deg]. The difference between the two angles is due to the chamber being larger in the latter case.

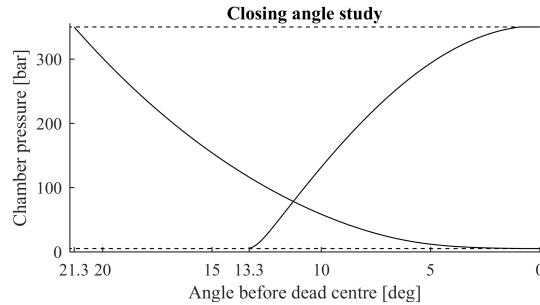


Figure 3.1: Necessary closing angle for the chamber to properly pressurise for both valves.

This corresponds to a flow of $1 - \cos(\theta_c)$ or approximately 3% and 7% of the maximum flow rate, respectively.

Secondly, the spring force is modelled as a constant force meaning the spring stiffness is zero. This, of course, is not physically possible, however, it is considered a good ideal case since there is little advantage in increasing the opposing the spring force while closing the valve. This constant force is set as 10 % above the maximum fluid force to add some safety margin which ensures that the valve does not close at maximum flow.

Although the switching time is a good and intuitive measure the fluid power losses during switching, there is a difference between the valve closing a little, then stopping, then closing totally, and the valve closing a little before slamming shut even though these may have the same switching time. This effect can be seen in Figure 3.2. This yields an objective function given by

$$\text{Switching loss } O_2 = \int_{t_0}^{T_s} \Delta p Q_{\text{closing}} dt \quad (3.3)$$

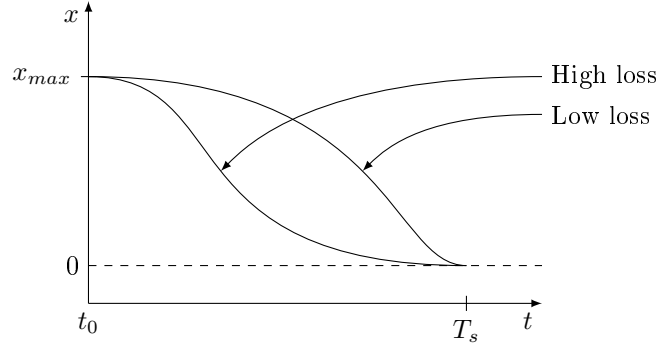


Figure 3.2: Different fluid power loss at the same switching time.

3.1.3 | Electric power consumption

The last objective is included to reduce the electrical power consumption when switching. This is done by integrating the electrical power when current is carried through the coil and will penalise a design with a long current rise time. This yields the expression

$$\text{Electrical power: } O_3 = \int_{T_{rev}} \Delta p(Q) Q(t) dt. \quad (3.4)$$

3.1.4 | Summary

The three object functions are summarised by

$$\text{Objective 1: Pressure drop } O_1 = \int_0^{max}, \quad (3.5)$$

$$\text{Objective 2: Switching loss } O_2 = \int_{t_0}^{T_s} \Delta p Q_{\text{closing}} dt, \quad (3.6)$$

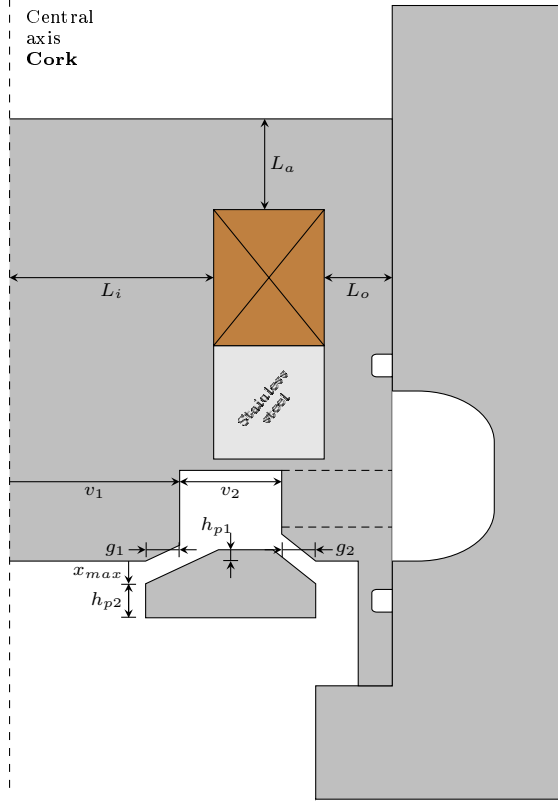
$$\text{Objective 3: Electric energy } O_3 = \int_0^T v(t) i(t). \quad (3.7)$$

$$(3.8)$$

Minimising these object functions will result in a, if possible, energy efficient valve with a low pressure drop, fast switching time, and relatively low requirements to the power supply.

3.2 | Design Variables

The design variables of the optimisation can be seen in Figure 3.3a as well as the number of turns in the coil, the relative opening of the outlet, and the angles of the sloped sides of the plunger.



(a) Design variables for the cork geometry.

Variable	Boundaries	Unit
v_1	[3; 20]	[mm]
v_2	[3; 20]	[mm]
g_1	[0.5; 2]	[mm]
g_2	[0.5; 2]	[mm]
x_{max}	[0.5; 5]	[mm]
α_1	[30; 60]	[°]
α_2	[30; 60]	[°]
h_{p1}	[-2; 2]	[mm]
h_{p2}	[2; 6]	[mm]
L_i	[8; 17]	[mm]
L_a	[5; 10]	[mm]
L_o	[4; 7]	[mm]
N	[50; 300]	[-]
g_{s1}	[0.1; 0.9]	[-]

(b) Lower and upper boundary for design variables.

3.3 | Optimisation

Due to the multiple object functions a generic algorithm is used to minimise the problem. This section will cover the method used to evaluate a single design as well as the structure of the entire optimisation algorithm.

3.3.1 | Function evaluation

Due to the long evaluation time of a single design, which includes two 2D CFD simulations, twenty eight 2D FEA simulations, and two transient simulations, the ability to determine whether a design is good or not is essential early in the function evaluation so that all steps are not necessary. Therefore, return functions are key components of the function evaluation.

The evaluation is broken into different steps, some of which will end the function evaluation if the design is deemed a failure, and can be seen below.

1. All design variables are checked to be within the predefined lower and upper boundary specified. If one variable is not within these boundaries the evaluation will terminate.
2. It is checked whether or not the designs geometry reasonable. An example of an unreasonable design could

be if the distances L_i and L_o added up to more than the radius of the valve. The aspects considered are $L_i + L_o > R$, $v_1 + v_2 + g_2 > R_i$, $-h_{p1} > x_{max}$, and the resting surface described in Section 2.4. If any of these aspects fail the evaluation is terminated. Furthermore, the wire diameter and resistance are calculated in this step as well as the maximum current.

3. A single electromagnetic FEA analysis is run to determine the static actuator force when the valve is fully opened and the maximum current is running through the coil. If this force is low (below 20 [N]) there is no reasonable chance of the valve closing, much less closing quickly. If the force is below 20 [N] the evaluation is terminated.
4. The pressure drop and flow force are found at the maximum flow rate. The pretension of the spring is defined as 10 % more than the maximum flow force. If the spring force is greater than the closing force described in the last step the evaluation is terminated. If not the pressure drop and flow force are found at half the maximum flow rate to obtain the two points needed for the quadratic approximation described in Section 2.3.2.
5. The position and current dependent actuator force and inductance are mapped by sweeping through various positions and magnetomotive forces. As can be seen in Figures 2.6 and 2.7 most changes occur a relatively low magnetomotive force and therefore the data points are more concentrated in this area. This is done by linearly spacing the cube roots of Ni and the cubing this vector of values, i.e. $[\sqrt[3]{\varepsilon_1}, \sqrt[3]{\varepsilon_2}, \dots, \sqrt[3]{\varepsilon_n}]^3$ where $\varepsilon_{1..n}$ are equally spaced.
6. The dynamic simulation is done in two steps. The first step calculates the first object function by simulating the oil flow of a single revolution through one valve. The second step starts with the valve open and a current of zero. The current reference is then set to the maximum current of the PSU and adjusts the voltage appropriately using a simple high gain P-controller and limiting the voltage to plus/minus the maximum voltage of the PSU. The current increases causing the actuator force to increase until it surpasses the opposing spring force minus the fluid force at the flow rate when the valve is closing. When the actuator surpasses this force, the plunger moves towards the closed position. When the plunger is fully closed the current reference is set to zero and the simulation continues until this has been reached. Through this second step the two last objective functions can be calculated, successfully concluding the function evaluation of this specific design.

If the design returned, without going through all steps, it was assigned an appropriately high function value depending on how many steps it got through with the least steps having the highest function value.

3.3.2 | Optimisation algorithm

The optimisation algorithm is a simplification of the popular algorithm Generic Differential Evolution (GDE) as described in [11]. The two methods differ in that GDE relies on an entire generation before determining which designs will continue and crossover is included, where as the simplified version is explained by

1. Generate one comparing parent, one main parent, and two supportive parents.
2. Generate the child according to $c = p_{main} + F(p_{sup,1} - p_{sup,2})$.
3. Calculate function value for the child.
4. If the objective function value of the child is smaller than the objective function value of the comparing, for all objective functions, the child takes the spot of the comparing parent in the population. The cycle starts over.

This method has both advantages and disadvantages compared to the traditional GDE. The advantage is that successful designs get quicker implemented into the population from which the children are made of. The disadvantage is that not all designs will have the opportunity of being a main parent before being replaced. This is key for keeping the population diverse and helps decrease the likelihood of the population converging to a local minimum.

In order to verify that the population stayed diverse the design variables were regularly plotted using the `ksdensity`-function in Matlab.

3.4 | Optimisation Results

Through the optimisation some candidate designs were found and the best designs for each object function is shown below as well as some general tendencies which could help limit the number of design variables in future optimisations.

3.4.1 | Flow losses

This design with the lowest flow loss when kept fully open can be seen Figure 3.4. The primary keys to success for this design are the long travel distance of 3.4 [mm] and the big outlet which is at the upper boundary of 0.9 yielding a pressure drop of 0.4 [bar] at maximum flow.

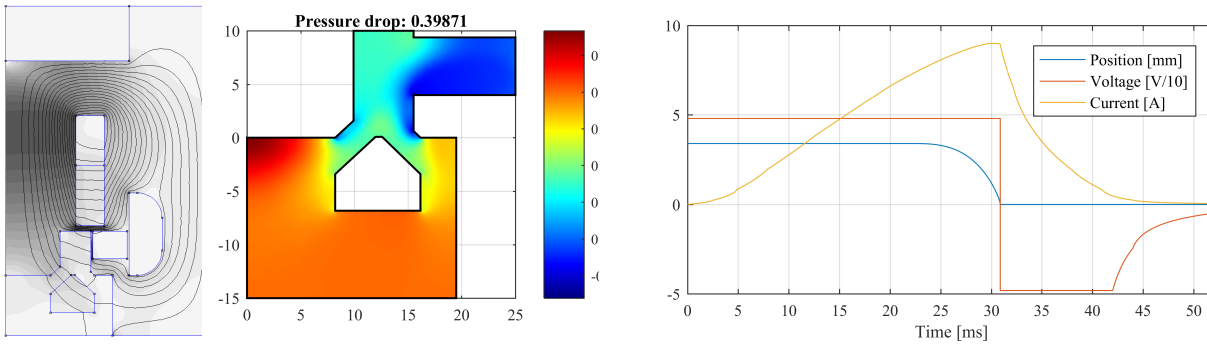


Figure 3.4: Design with lowest flow loss.

3.4.2 | Fluid power switching losses

This design has the lowest fluid power switching loss. This is most likely due to the large pressure drop just across the plunger meaning when the plunger starts closing it will rapidly start accelerating. Furthermore the plunger and moving mass only weigh 33.4 [gram] combined while the other two optimal designs weigh 40 [gram] and 49 [gram], respectively.

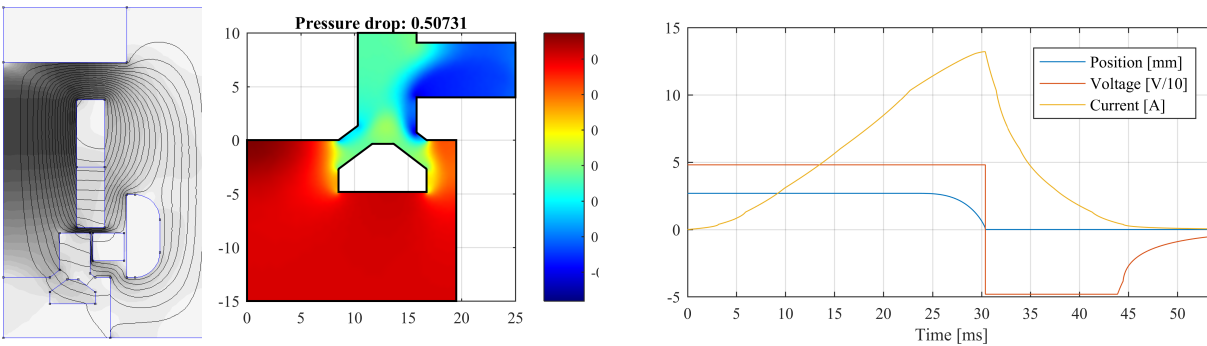


Figure 3.5: Design with lowest fluid power switching loss.

3.4.3 | Electric power consumption

The third design highlighted is the valve which consumed the least power electrically. As can be seen from the dynamic plot the current increases quickly until it reaches the current limit. Then the voltage drops so that

it just keeps the current of 20 [A] until there is enough force to close the valve. The small increase in voltage when the valve is just about to have closed is the back-EMF lowering the current under the current reference of 20 [A]. The key to success is the low resistance of only 0.61 [Ω] meaning the current will reach its maximum quickly allowing the voltage to drop. This means that the current and voltage are only both high for a short time meaning the product of the two is high for a short time only.

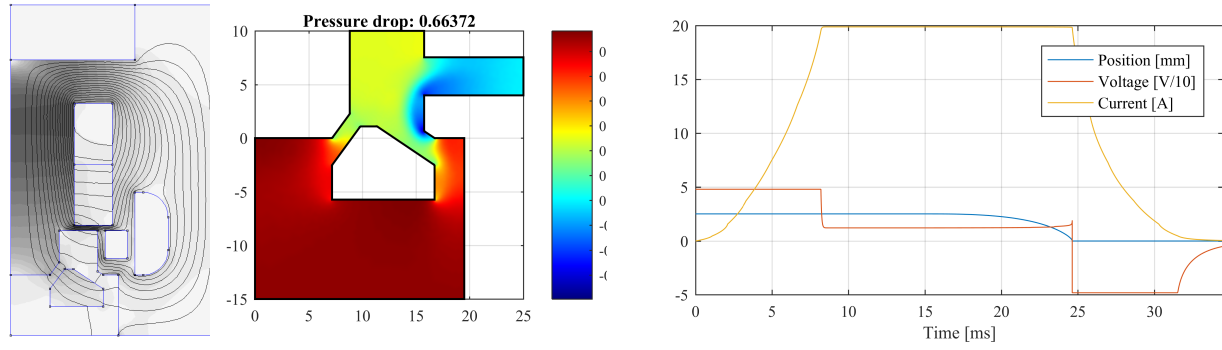


Figure 3.6: Design with lowest electrical losses.

4 | Experiment

As a proof of concept and to verify some of the modelling methods used a prototype, highly inspired by the project previous semester, was manufactured and tested outside the manifold. The valves transient performance was tested both in and out of oil.

4.1 | Prototype

The prototype has been designed in Solidworks and can be seen in Figure 4.1. It is designed so that it fits in the manifold of the experimental setup at Aalborg University which require two valves as seen in 4.2. This puts some restrictions on the diameter and height of the valve as well as the voltage and current ranges. It was found in the ninth semester that especially the diameter restriction was of importance and therefore the prototype is not ideal. This diameter limit means that the centre of the valve is prone to saturation meaning less flux is generated.

4.1.1 | Issues

Of course, no prototype design is perfect and even though a lot of thinking had gone into the design there are issues and improvements to be made for the next iteration of the solenoid valve. It is noted that, at the day of writing, the valve has not been under pressure nor has it been exhaustively impact tested. The issues found are

- Thread direction: Perhaps the most empty minded mistake in the design is to make all threads in the same direction. By doing so, the entire concept of screwing the valve into and out of the manifold is undermined since any attempt of unscrewing the valve will cause it to fall apart and leaving the core in the manifold. The idea was for the central bolt to press the coil plug to the core allowing the two to be screwed out of the manifold together. However, a simpler solution would be thread the coil plug and inside of the core in the opposite direction. This would mean that, as the valve is screwed into the manifold, it would tighten against the central bolt and as while screwing it out of the manifold it would tighten against the core.
- Fragile stop bolt: The stop bolt, keeping the plunger in place, is quite fragile and should be thickened or made of a stronger material, e.g. titanium. During the unnecessarily difficult disassembly, due to the abovementioned issue, it broke.
- Winding of the coil: The calculations describing the fill factor of the coil were found to be too idealistic. Even after adjusting for the less ideal world the fill factor was found to be considerably lower than expected. This error is possibly due to the coil being wound first in one direction and then in the other direction on the way back. Due to the wires constantly overlapping one another the hexagonal pattern was unobtainable and a simple square pattern would have been a better approximation.
- Machining difficulties: Two challenges during machining were highlighted by the workshop. One was the 0.5 [mm] thick aluminium coil holder which had to be machined at lower speeds due to its thinness. This could be resolved by omitting the holder entirely and instead wind the coil onto a temporary holder and then transfer it to the coil plug. The other difficult was the small holes through the side of the core which are hard to reach with the small drill bits needed. Manufacturing the part of the core below the reinforcement is possible without losing the alignment of the plunger-core resting surface, however, a

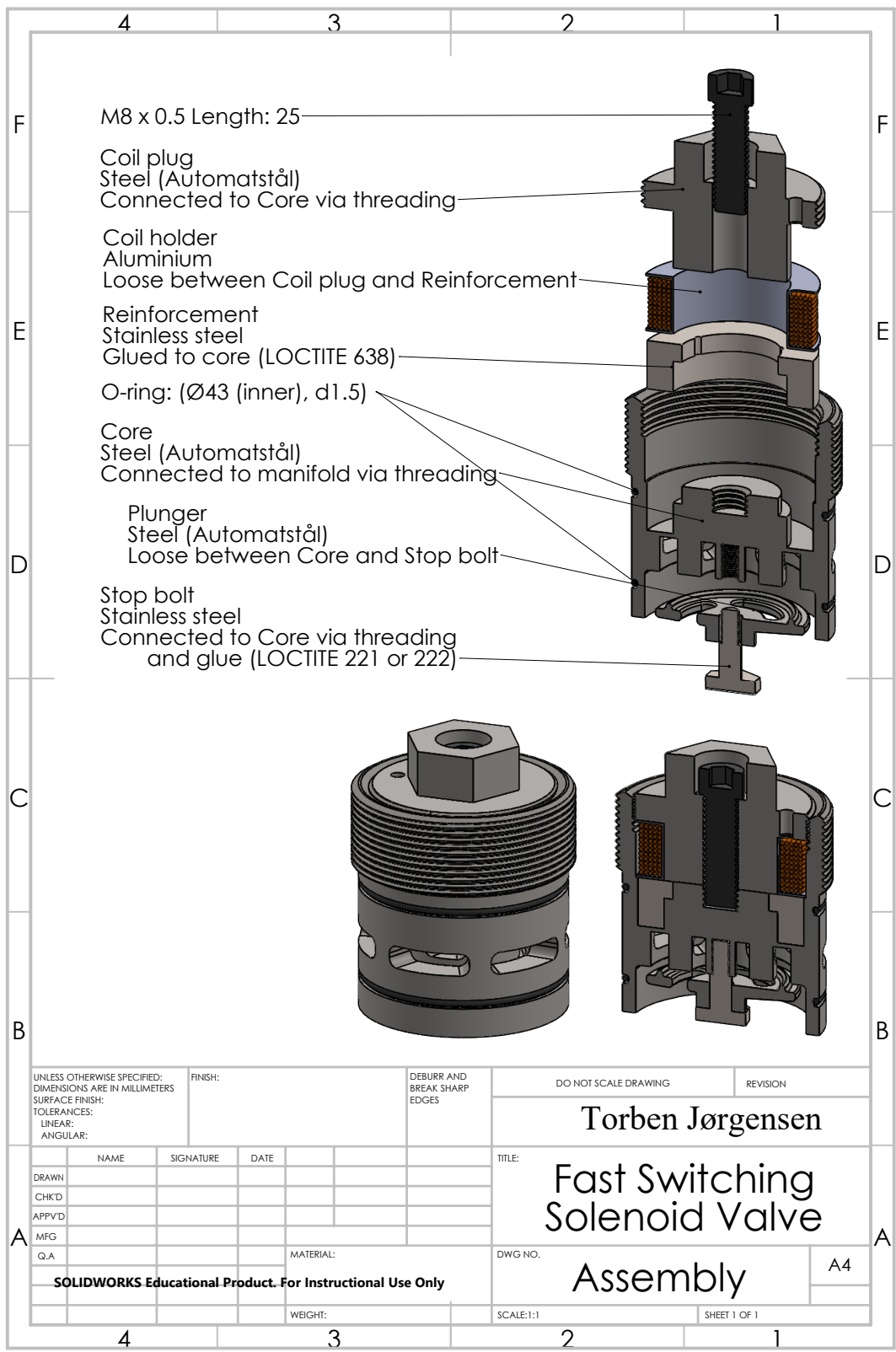


Figure 4.1: Solidworks drawing of the prototype assembly with each part annotated.

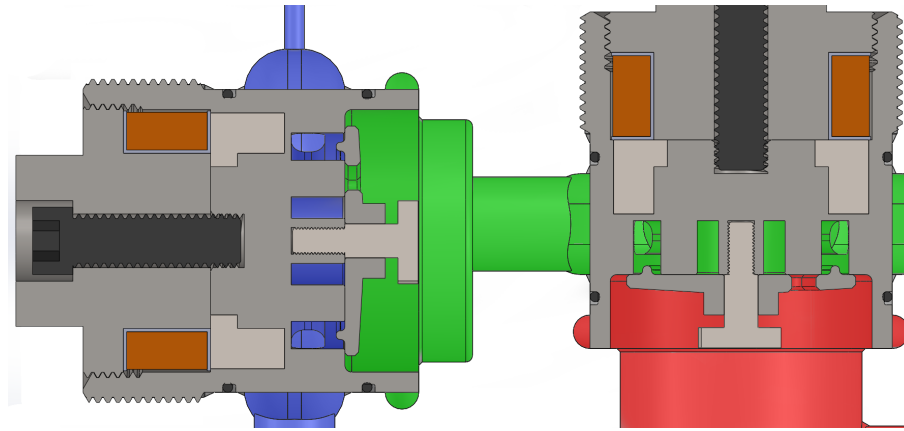


Figure 4.2: Manifold with the blue region being the LP oil, green region is manifold oil, and red is HP oil.

simpler solution would be to drill bigger holes through the side.

- Moving top o-ring: As mentioned in Section 2.4, about modelling of the mechanical stress, distance between the top o-ring and outside of the coil is critical. Due to the design of the, already manufactured, manifold the o-rings must be at a relatively fixed positions with respect to the bottom of the valve. If the top o-ring could be placed closer to the bottom it would leave more room for the coil.

4.2 | Experimental Setup

The switching speed of the valve was tested both out of and in oil. The voltage, current and distance were measured by probes connected to an oscilloscope. The valve was triggered using LabVIEW connected to an H-bridge which also connected the capacitor power bank to the coil of the valve. LabVIEW was setup to output a high pulse for a certain amount of time. It is noted that due to a breakdown in the original experimental the valve could not be run at 48 [V] but instead around 30 [V] with a current limit of 10 [A]

A photo of the valve submerged in oil can be seen in Figure 4.3 and a video of the valve closing can be seen at <https://youtu.be/QmBgC97X2aY>.

4.3 | Experiment Results

Some interesting and unforeseen effects were observed during the experiment. These unforeseen were

- Eddy currents lowering the effective inductance when the power is just turned on. This means that the current jumps to approximately 4 [A] when the voltage is just turned high. The way of modelling the eddy currents does not reflect this and therefore an improved way of modelling these is needed. If modelled correctly it would have a positive effect on the performance of the modelled valves.
- The plunger stuck to the stop bolt when the valve was tested in oil much more than anticipated. This not only meant that the plunger would start closing later it also meant that the valve would need a significantly higher voltage to close. The valve in air was able to close at 12 [V] but the valve in oil was not able to close at 20 [V]. The stiction effect can possibly be minimised by adding grooves on the under side of the stop bolt or over side of the plunger.
- There was no significant change in closing time between oil and air. Due to the aforementioned stiction effect the plunger waited longer before starting to move. This meant that the current and thereby actuator force would be greater when the plunger starts to move. This, by coincidence, cancelled out the effect of the added mass from the oil.

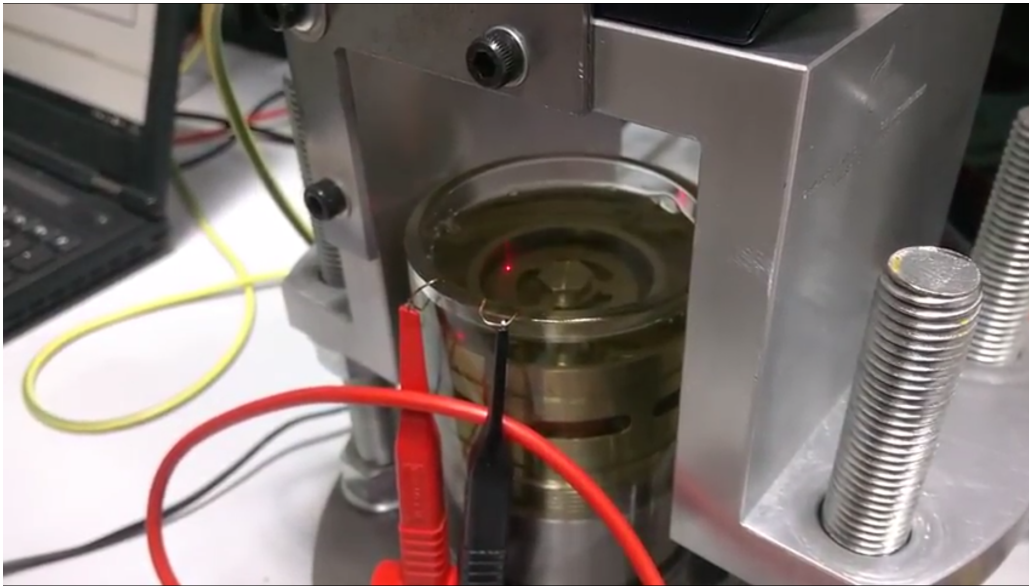


Figure 4.3: Photo of the valve submerged in oil.

A comparison between the oil and air test at 31.4 [V] can be seen in Figure 4.4 with the annotated points of interest. The primary take-away from these results are

- The modelled eddy current does not reflect the real effect that the eddy currents have. A different model must be made to accurately capture these dynamics.
- The stop bolt or plunger must be redesigned so that the stiction effect has less effect on the delay between turning on the power and the plunger starting to move.

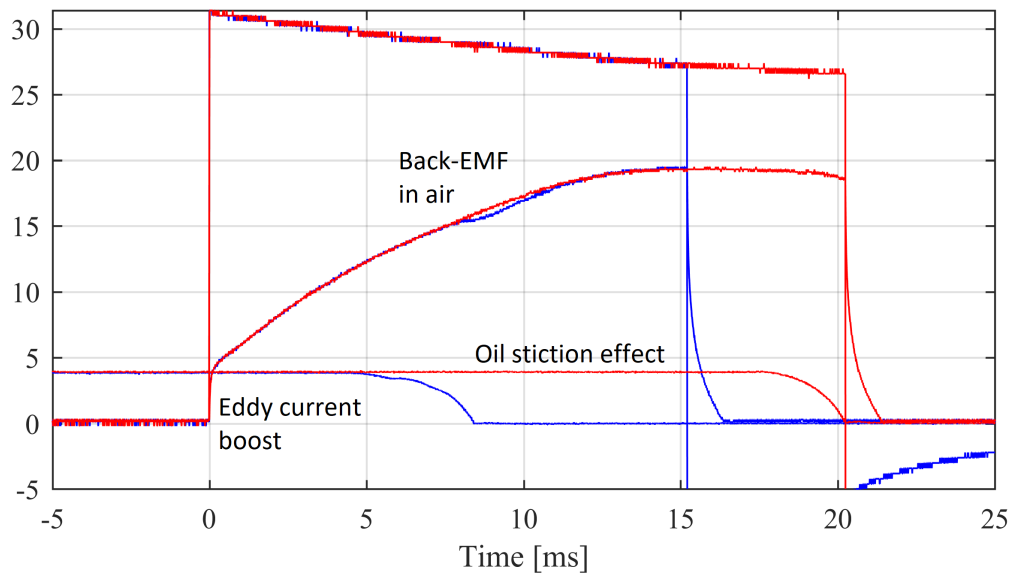


Figure 4.4: Oil (red) and air (blue) comparison.

5 | Conclusion

With mixed results the proposed design has been modelled, optimised, and tested. Pole shaping has been which made it possible to achieve travel distances above 3 [mm] and still function. This lead to modelled pressure drops below 0.4 [bar] at maximum flow.

The modelling was done using multiple numerical methods used with care and tested for mesh independence. The resulting fluid dynamic and electromagnetic maps were used in an optimisation which had the purpose of finding efficient designs. It did so by minimising three object functions describing the fluid power loss when not switching, fluid power loss when switching, and electric power consumption when switching. These resulted in some optimised design which were show cased. For flow efficiency the travel distance and outlet size were greater than average yielding a pressure drop of 0.4 [bar]. The fluid power loss during switching was primarily dominated by the plungers weight and the pressure drop directly across the plunger. The electrically efficient design has a small resistance leading its current to increase rapidly until the reference was met enabling the voltage to be lower for the majority of the electrical switching time.

All design, however, still suffers from a long switching time which is undesirable for multiple reasons. First and foremost it has been shown, although under questionable assumptions that it has a poor effect on the efficiency of the transmission. Secondly, it would cause the valve to be harder to control due to the increased delay between voltage input and the output which is the plunger closing.

Experimentally a discrepancy was found in the modelling of eddy currents which must be resolved before the model can be deemed precise enough. Furthermore, some design flaws were found during manufacturing including threading direction and component strength.

The model also did not reflect the stiction effect found experimentally, however, design alternatives may be able to minimise this effect.

To conclude, the performance of the solenoid valve is still not on par with state of the art fast switching valves and further work or new ideas are needed for the solenoid to compete with more advanced topologies.

Further work

To take this project to the next level some steps must be taken. These include

- Redesigning the stop bolt to minimise the stiction effect and strengthen it. The threading must also be reversed at one place to ease disassembly with the manifold.
- Eddy currents must be modelled to reflect the experience gotten through experiments.
- More elaborate data analysis is needed to verify the other submodels and further testing is needed, e.g. pressure drop test, and mechanical stress test.

Bibliography

- [1] Denmark Institute of Machine Design Department of Energy Technology, Aalborg University (ET-AAU) and Austria-Austrian Center of Competence in Mechatronics (ACCM) Austria Bosch Rexroth A/S (BR) Denmark/Germany MHI Vestas Offshore Wind Denmark Wave Star A/S (WS) Denmark Hydraulic Drives, Johannes Kepler Universitat (JKU). Hydrive.et.aau.dk, April 2014 - April 30 2019. URL <http://www.hydrive.et.aau.dk/about/>.
- [2] A. G. Drachmann. Heron's windmill, 1961.
- [3] Yunus engel. *Fundamentals of thermal-fluid sciences*. McGraw-Hill Higher Education, New York, 2012. ISBN 978-007-132511-0.
- [4] S. Gibson, G. W. Jewel, and R. E. Clark. Variable-airgap, cylindrical, linear variable reluctance actuators for high-force, medium-stroke applications. *IET Electric Power Applications*, 3(4):352–362, July 2009. ISSN 1751-8660. doi: 10.1049/iet-epa.2006.0304.
- [5] Sunghun Kim and Hubertus Murrenhoff. Measurement of effective bulk modulus for hydraulic oil at low pressure. *Journal of Fluids Engineering*, 134(2):021201, 2012. doi: 10.1115/1.4005672. URL <https://doi.org/10.1115/1.4005672>.
- [6] Christian Nørgård, Michael Møller Bech, Daniel Beck Roemer, and Henrik Clemmensen Pedersen. Optimization of moving coil actuators for digital displacement machines, 5 2016.
- [7] Artemis Intelligent Power. URL <http://www.artemisip.com/>. Accessed: 16-02-2017.
- [8] W.H.S. Rampen, N.J. Caldwell, and U.B.P. Stein. Valve actuator, October 20 2011. URL <http://www.google.ch/patents/US20110253918>. US Patent App. 13/126,631.
- [9] Daniel B. Roemer. *Design and Optimization of Fast Switching Valves for Large Scale Digital Hydraulic Motors*. PhD thesis, Department of Energy Technology Aalborg University Pønstoppidanstræde 101 DK-9220 Aalborg East Denmark, 2015.
- [10] U.B.P. Stein. Fluid-working machine, June 24 2014. URL <https://www.google.ch/patents/US8757583>. US Patent 8,757,583.
- [11] Rainer Storn and Kenneth Price. Differential evolution – a simple and efficient heuristic for global optimization over continuous spaces. *Journal of Global Optimization*, 11(4):341–359, 1997. ISSN 1573-2916. doi: 10.1023/A:1008202821328. URL <http://dx.doi.org/10.1023/A:1008202821328>.
- [12] Kazuhisa Tsutsumi, Atsushi Maekawa, Masayuki Shimizu, Stephen Salter, Uwe Stein, William Rampen, Robert Fox, and Hauke Karstens. Wind turbine generator and tidal current generator, 2012. URL <https://patents.google.com/patent/US20120061969A1/en>.
- [13] Dick Yue. 2.20 marine hydrodynamics (13.021). spring 2005. massachusetts institute of technology. MIT OpenCourseWare, <https://ocw.mit.edu>. License: Creative Commons BY-NC-SA. URL http://web.mit.edu/fluids-modules/www/potential_flows/LecturesHTML/lec12/node1.html.

BIBLIOGRAPHY

A | Modelling

A.1 | Electromagnetic Characteristic Mapping

To model the actuator performance dynamically the inductance and force are wanted at multiple positions and currents. This modelling is done using FEMM which is a 2D static finite element solver which uses two of Maxwell's equations given by

$$\begin{aligned} \text{Gauss's law for magnetism: } \nabla \cdot \mathbf{B} &= 0 \\ \text{Ampère's law: } \nabla \times \mathbf{B} &= \mu(\mathbf{B})J. \end{aligned} \tag{A.1}$$

Due to possible adjustments in the optimisation dependent on its performance the characterisation is attempted generalised with respect to the number of turns. Therefore, the actuator force, inductance, and inductance gradient is found at different positions, x , and magnetomotive forces, ε , for a single turn coil.

The force is not strictly dependent on the number of turns but only the magnetomotive force since the force at 1 [A] and 100 turns is equal that at 100 [A] and a single turn. Hence, it is a simple matter of mapping it with respect to the magnetomotive force.

The inductance, however, is slightly more difficult since the inductance at 1 [A] and 100 turns is not equal that at 100 [A] and a single turn. From the expression $L = \frac{N^2}{\mathcal{R}(x,\varepsilon)}$ it is seen that the inductance is proportional to the number of turns squared, yielding

$$L = N^2 L(x, \varepsilon_{N=1}). \tag{A.2}$$

where the value inductance at a single turn is obtained as the flux per current parameter found through FEMM.

To find the inductance gradient one could simply take the numerical spatial derivative of the inductance, however, by doing so one would lose a data point. Instead the gradient is found through the force-work relation and the energy in an inductor which are given by

$$F = \frac{\partial W}{\partial x} \quad \text{and} \quad E = \frac{1}{2} L(x, \varepsilon) i^2. \tag{A.3}$$

By substituting the energy of the inductor into the force-work relation and rearranging the force is given by

$$F(x, \varepsilon) = \frac{i^2}{2} \frac{\partial L(x, \varepsilon)}{\partial x}, \tag{A.4}$$

from where the inductance gradient can be isolated and is given by

$$\frac{\partial L(x, \varepsilon)}{\partial x} = \frac{2F(x, \varepsilon)}{i^2}. \tag{A.5}$$

Lastly, as previously described, the inductance is proportional to the number of turns squared so in order to map the inductance gradient for a single turn it is defined as

$$\frac{\partial L(x, \varepsilon_{N=1})}{\partial x} = \frac{2F(x, \varepsilon)}{i^2 N^2}. \tag{A.6}$$

APPENDIX A. MODELLING

When these mapped values are used in Simulink it is important to remember scaling the inductance and inductance gradient to fit the appropriate number of turns. This means that the typical voltage equation for a LR-circuit given by

$$v = Ri + L(x, \varepsilon) \frac{\partial i}{\partial t} + i \frac{\partial L(x, \varepsilon)}{\partial x} \frac{\partial x}{\partial t} \quad (\text{A.7})$$

is substituted with

$$v = Ri + N^2 \left(L(x, \varepsilon_{N=1}) \frac{\partial i}{\partial t} + i \frac{\partial L(x, \varepsilon_{N=1})}{\partial x} \frac{\partial x}{\partial t} \right) \quad (\text{A.8})$$

where $L(x, \varepsilon_{N=1})$ and $\frac{\partial L(x, \varepsilon_{N=1})}{\partial x}$ are the values found through FEMM.

A.2 | Coil Characterisation

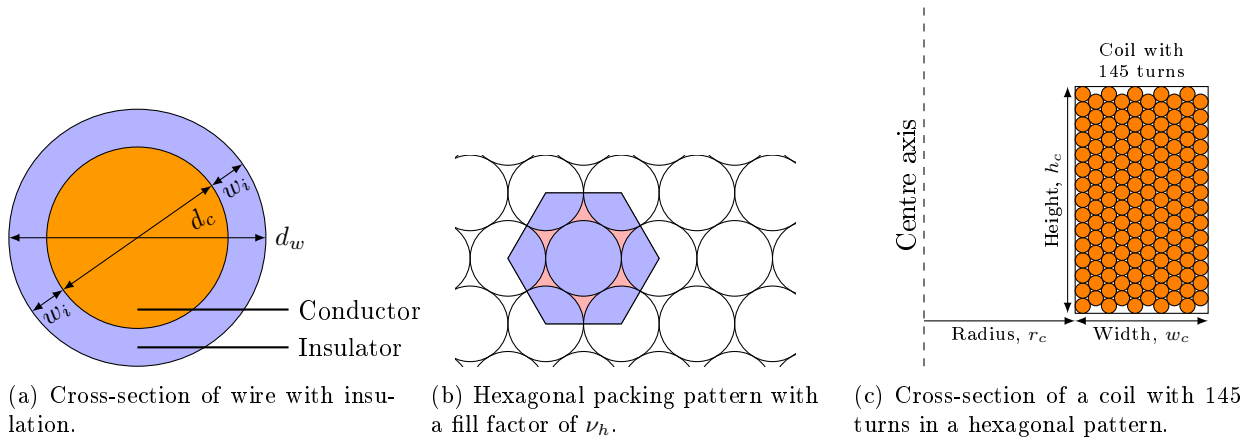
The coil will be characterised with respect to the fill factor and the maximum current for the coil not to overheat.

A.2.1 | Fill Factor

Since round wires are chosen for the coil some waste space in between the windings is unavoidable. This wasted space can be described by a wire fill factor, ν_w , which depend on the number of turns, n , which is analogous to a packing efficiency. This is given as

$$\nu_w = \frac{n \frac{\pi}{4} d_w^2}{w_c h_c} \quad (\text{A.9})$$

where d_w is the wire diameter, and h_c and w_c is the height and width of the coil as seen in Figure A.1c. The wire consists of a conducting centre coated in an insulating material which ensures that when the wire is wound into a coil there is no short circuits between the turns. Therefore, the wire diameter is described by $d_w = d_c + 2w_i$ which is visualised in Figure A.1a. The wasted space between the wires is described by using circle packing data

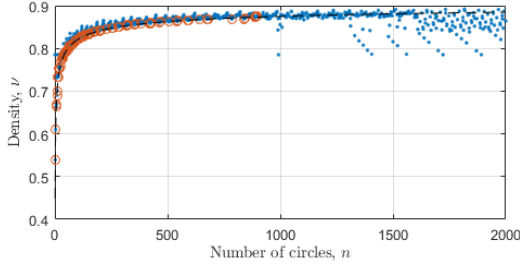


for identical circles packed in a square. This is considered a good approximation for identical circles packed in a rectangle since the packing pattern for most cases closely resemble the hexagonal or honeycomb pattern which is expandable in both the horizontal and vertical direction. This hexagonal pattern can be seen in Figure A.1b. As the number of circles grow the fill factor approaches the density described by of Thue's theorem which is given by $\nu_h = \frac{\pi}{\sqrt{12}} \approx 0.90690$. This value can further be seen as the ratio between the blue area and the coloured hexagon in Figure A.1b. However, for a finite number of circles fitted into a square this density not achievable and the equation describing the fill factor for these cases is instead approximated from data from <http://hydra.nat.uni-magdeburg.de/packing/csq/csq.html#overview>. Figure A.2a shows this data up to approximately 2000 circles, however, it is noted that from about 1000 circles the data seems to diverge, likely, due to the pattern not being optimal. Therefore a fit is made for n below 900. To capture the worst case scenario

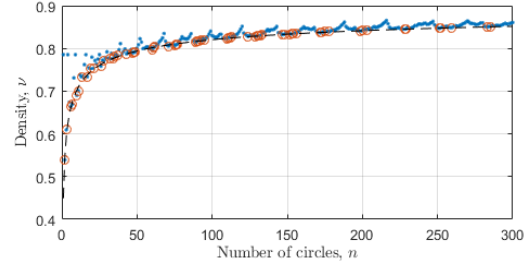
better the lower boundary of the data is approximated. This is done by ignoring the point if a point exists which has more circles and a lower density which are encircled in red in Figure A.2a. This data is fitted using the power law with an offset which is given by

$$\nu_w = an^b + c, \text{ where } a = -0.473, b = -0.334, \text{ and } c = 0.922. \quad (\text{A.10})$$

The resulting fit, up to 300 circles, can be seen in Figure A.2b. Since an explicit expression, for the conductor



(a) Circle density study up to 2000 circles showing a significant divergence from tendency for the first 1000 circles.



(b) Circle density study up to 300 circles.

diameter as a function of the coil area and number of turns, is wanted Eq. A.9 is combined with the definition of the wire diameter and the fitted power law thereby yielding

$$d_c = \frac{2\sqrt{w_c h_c \nu_w(n)}}{\sqrt{(\pi n)}} - 2w_i \quad (\text{A.11})$$

A.2.2 | Maximum Current

The maximum current through a conductor with diameter, d_c , will be analysed by assessing the temperature increase through one cycle. To simplify this calculation it is assumed that the coil does not transfer any heat to the core. This is also the worst case scenario. The heat-energy added to the coil is described by the integrating the power loss of a conductor given by

$$Q_{coil} = \int P_{coil} dt = \int R(T) i^2 dt \quad (\text{A.12})$$

where $R(T)$ is the temperature dependent resistance of the coil and i is the current passing through the coil. The resistance is given by

$$R(T) = \rho(T) \frac{L_{coil}}{A_{coil}} \quad (\text{A.13})$$

where L_{coil} is the length of the wire, A_{coil} is the cross-sectional area of the coil, and $\rho(T)$ is the temperature dependent resistivity defined by $\rho(T) = \rho_{cu} (1 + \alpha_{cu} (T - T_{cu}))$. The coefficients for copper at a base temperature of $T_{cu} = 20^\circ\text{C}$ are $\rho_{cu} = 1.68 \times 10^{-8}$ and $\alpha_{cu} = 3.862 \times 10^{-3}$, i.e. a temperature increase of $10 [^\circ\text{C}]$ will cause the resistivity to increase by little under four per cent. However, since the temperature should not increase drastically over the duration of a single cycle and α_{cu} being relatively low the resistivity is assumed constant.

The temperature increase of the coil is described using the thermal heat capacity given by

$$\Delta T = \frac{Q_{coil}}{c_{p,cu} m_{coil}}, \quad (\text{A.14})$$

where $c_{p,cu}$ is the mass specific heat capacity of copper, and m_{coil} is the mass of the coil given by the product of the mass density, length, and area of the conductor.

APPENDIX A. MODELLING

Combining the power loss of the coil and the temperature increase expression as well as defining the conductor area and mass of the coil yields

$$\Delta T = \frac{R}{c_{p,cu} m_{coil}} \int i^2 dt = \frac{\rho_T \frac{L_{coil}}{A_{coil}}}{c_p \rho_m L_{coil} A_{coil}} \int i^2 dt = \frac{\rho_T}{c_{p,cu} \rho_m \left(\frac{\pi}{4} d_c^2\right)^2} \int i^2 dt = \frac{16}{\pi^2} \frac{\rho_T}{c_{p,cu} \rho_m} \frac{1}{d_c^4} \int i^2 dt, \quad (\text{A.15})$$

revealing that a temperature increase is highly sensitive to the conductor diameter. In fact halving the conductor diameter gives 16 times the temperature increase. It is further noted that $\Delta T \propto \int i^2 dt$ showing the importance of keeping the current low to avoid overheating the coil.

A.3 | Mesh Dependence for Numerical Methods

To simulate the valve several numerical methods are utilised, namely Finite Element Analysis and Computational Fluid Dynamics. Both of these methods depend on the mesh resolution with a finer mesh generally yielding a better approximation of the exact solution. However, the finer mesh comes at the cost of a longer computation time and, to a smaller extent, a higher memory usage. Since this is the case there is a trade-off between correctness and simulation time and therefore an adequate resolution must be found.

To find this adequate resolution a series of test designs, ten cork designs and ten tap designs, have been designed and can be seen in Table B.1.

Since the two numerical methods are done in FEMM and Comsol the metric for the mesh resolution is slightly different. In FEMM the mesh resolution is defined from a minimum inside angle at the corner of each triangle which constitute the mesh. This difference can especially be seen near nodes or lines of the geometry. Comparison between the average and the two extremes in FEMM, 10°, 20°, and 30°, can be seen in Figure A.3 where it is obvious that there are more elements (intersecting black lines), yielding a longer simulation time. It is noted that the figure illustrates its impact near nodes and lines is more significant than in a more open region so the many doubling of elements is not to be generalised, however, it illustrates the principle.

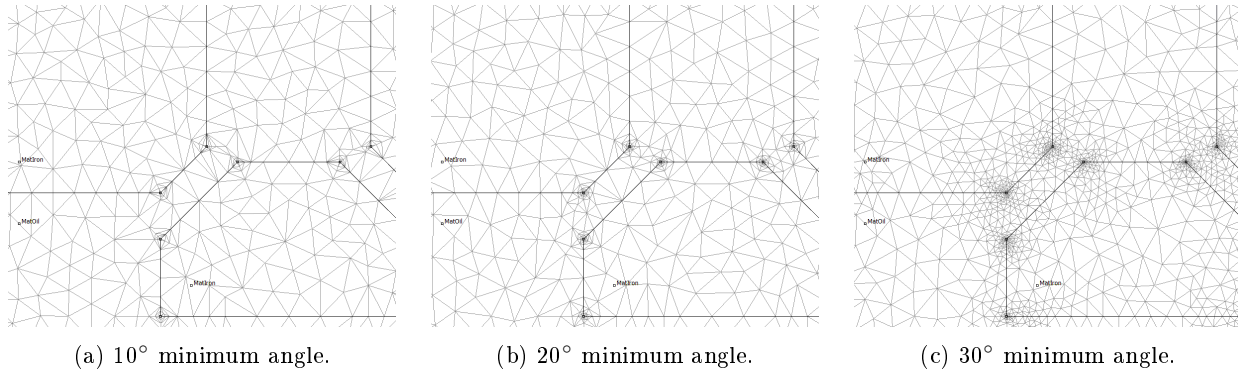


Figure A.3: Minimum angle comparison in FEMM.

This resolution range has been studied with respect to the actuator force and inductance and illustrated in Figure A.4. In said figure it is shown that for this case the poorest resolution is sufficient with a deviation within ± 4 [%] for the actuator force, and $\pm_{0.2}^0$ [%] for the inductance. It is further seen that the average simulation at 30 [°] is 2.7 [s] and 1.9 [s] at 10 [°] meaning a reduction of approximately 30 [%] in simulation time. The advantage of a faster simulation time is determined to outweigh the imprecisions caused by a poorer mesh. Since the geometry is already simplified, by exploiting the almost axisymmetric shape and therefore projecting it from 3D to 2D axisymmetric. This simplification is assumed to have a greater impact than the 4 [%] deviation stemming from the mesh resolution.

SECTION A.3. MESH DEPENDENCE FOR NUMERICAL METHODS

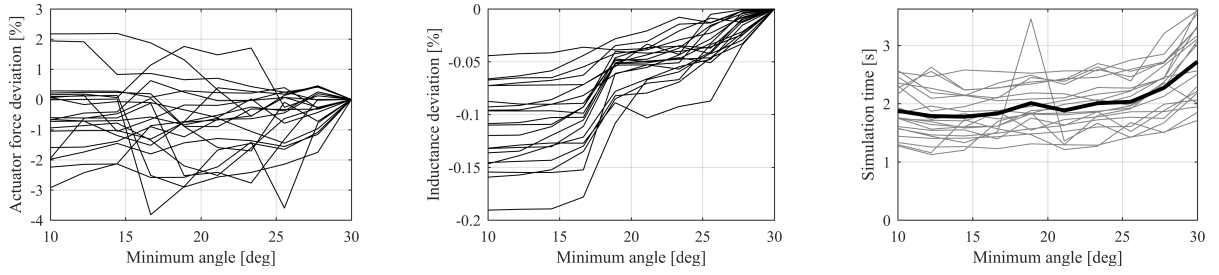


Figure A.4: Actuator force and inductance comparison, and the average simulation time for each resolution.

Controlling the mesh resolution in Comsol seems slightly more user-friendly, however, less quantifiable. The normal and extreme settings of Comsol can be seen in Figure A.5 where it is noted that the difference between the two extremes is relatively larger than that of the two extremes in FEMM.

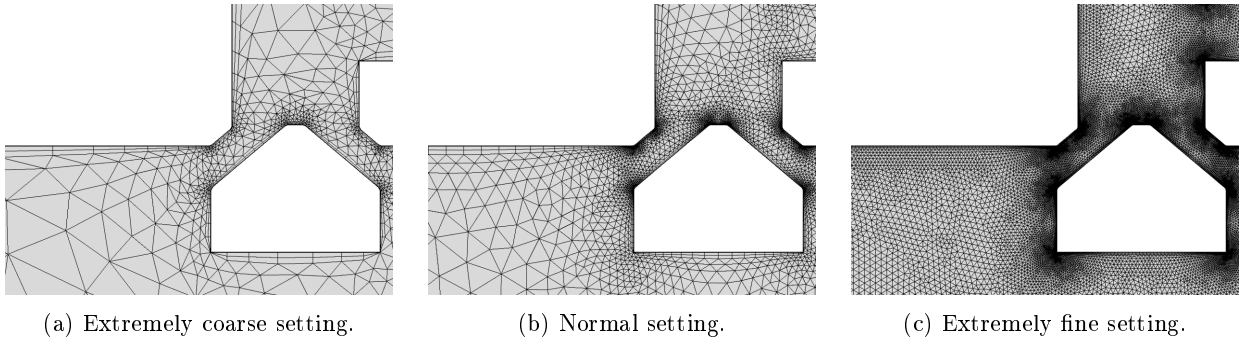


Figure A.5: Comsol mesh resolution at different settings.

Studying this resolution range has shown that there is little advantage to choosing a finer mesh, as shown in Figure A.6. It shows a deviation of \pm_{5}^{18} [%] for the pressure drop, and \pm_{2}^{6} [%] for the flow force. Again, this precision comes at the cost of a greatly increased simulation time to approximately the tenfold. As was the case in the electromagnetic mesh dependence the impact of projecting the geometry from 3D to 2D is assumed to be greater than the resolution related deviation.

This precision at a poor mesh resolution most likely stems from the simplified physics involved. Since the flow is assumed laminar and the fluid to be incompressible, i.e. non changing density, which greatly simplifies the equations involved and removes several non linearities. Furthermore, the geometry is relatively simple with only one obstruction between the single inlet and single outlet. One could argue that if the poorest mesh would not be sufficient for this problem it would be difficult to find a problem where it actually was sufficient.

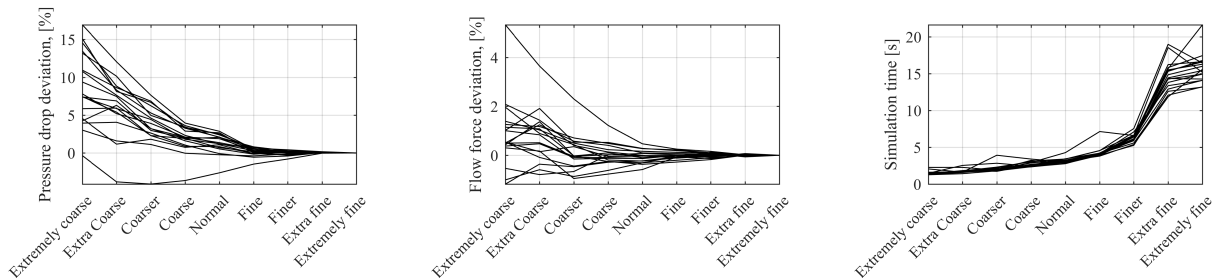
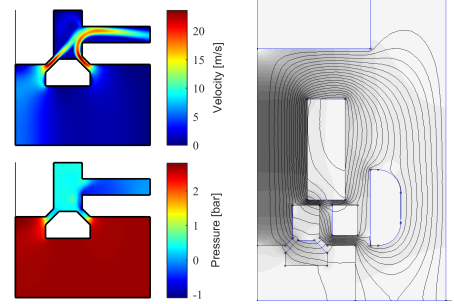


Figure A.6: Pressure drop, flow force, and simulation time for each resolution setting.

B | Test population

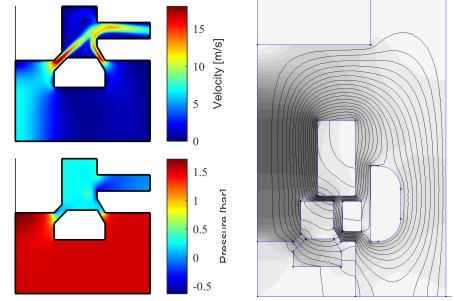
Type: Cork, Number: 1

$v_1 = 7.09$, $v_2 = 5.32$, $g_1 = 1.5$, $g_2 = 1.5$, $x = 1.5$,
 $\alpha_1 = 45$ [deg], $\alpha_2 = 45$ [deg], $h_{p1} = 1$, $h_{p2} = 2.5$,
 $L_i = 10$, $L_a = 10$, $L_o = 5$
 $\Delta p = 2.69$ [bar], $F_f = 104.76$ [N], $F_{act} = 78.22$ [N]



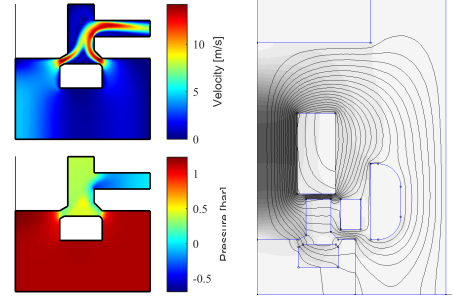
Type: Cork, Number: 2

$v_1 = 8.67$, $v_2 = 6.50$, $g_1 = 1.5$, $g_2 = 1.5$, $x = 2$,
 $\alpha_1 = 45$ [deg], $\alpha_2 = 60$ [deg], $h_{p1} = 0.5$, $h_{p2} = 3$,
 $L_i = 12$, $L_a = 15$, $L_o = 3$
 $\Delta p = 1.53$ [bar], $F_f = 83.03$ [N], $F_{act} = 134.61$ [N]



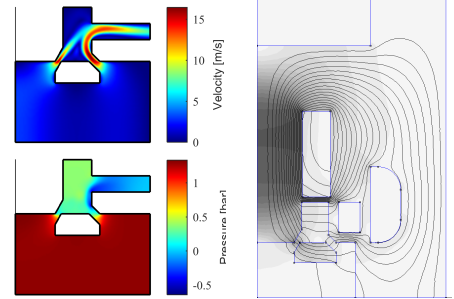
Type: Cork, Number: 3

$v_1 = 9.75$, $v_2 = 4.88$, $g_1 = 1.5$, $g_2 = 1.5$, $x = 1.5$,
 $\alpha_1 = 30$ [deg], $\alpha_2 = 45$ [deg], $h_{p1} = -1$, $h_{p2} = 4$,
 $L_i = 8$, $L_a = 14$, $L_o = 7$
 $\Delta p = 1.15$ [bar], $F_f = 45.70$ [N], $F_{act} = 27.54$ [N]

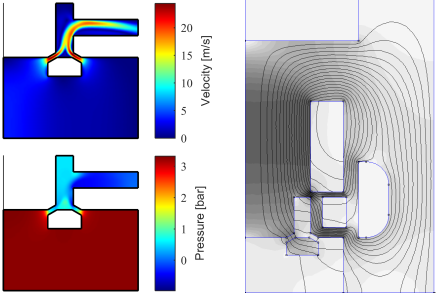
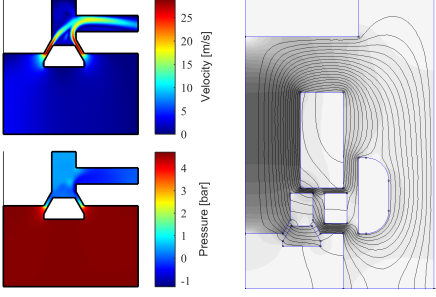
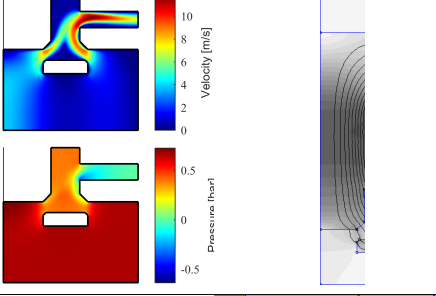
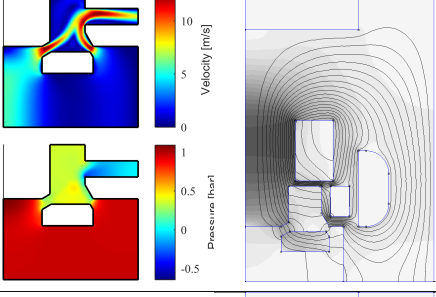
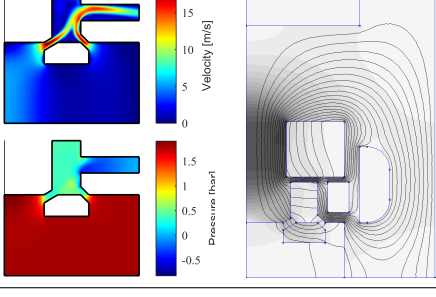


Type: Cork, Number: 4

$v_1 = 8.86$, $v_2 = 5.32$, $g_1 = 1.5$, $g_2 = 1.5$, $x = 2$,
 $\alpha_1 = 60$ [deg], $\alpha_2 = 45$ [deg], $h_{p1} = 0$, $h_{p2} = 2$,
 $L_i = 9$, $L_a = 13$, $L_o = 8$
 $\Delta p = 1.30$ [bar], $F_f = 55.41$ [N], $F_{act} = 54.90$ [N]

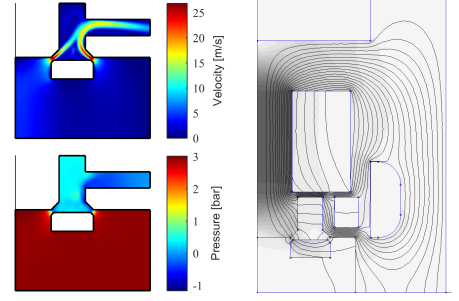


APPENDIX B. TEST POPULATION

<p>Type: Cork, Number: 5 $v_1 = 9.75$, $v_2 = 3.25$, $g_1 = 1.5$, $g_2 = 1.5$, $x = 1$, $\alpha_1 = 30$ [deg], $\alpha_2 = 30$ [deg], $h_{p1} = 0$, $h_{p2} = 2.5$, $L_i = 13$, $L_a = 12$, $L_o = 3$ $\Delta p = 3.27$ [bar], $F_f = 110.10$ [N], $F_{act} = 117.33$ [N]</p>	
<p>Type: Cork, Number: 6 $v_1 = 9.00$, $v_2 = 4.50$, $g_1 = 1.5$, $g_2 = 1.5$, $x = 1.5$, $\alpha_1 = 60$ [deg], $\alpha_2 = 60$ [deg], $h_{p1} = 1.5$, $h_{p2} = 1$, $L_i = 11$, $L_a = 11$, $L_o = 3$ $\Delta p = 4.65$ [bar], $F_f = 199.52$ [N], $F_{act} = 133.82$ [N]</p>	
<p>Type: Cork, Number: 7 $v_1 = 8.86$, $v_2 = 5.32$, $g_1 = 1.5$, $g_2 = 1.5$, $x = 2.5$, $\alpha_1 = 45$ [deg], $\alpha_2 = 45$ [deg], $h_{p1} = -2$, $h_{p2} = 2$, $L_i = 12$, $L_a = 16$, $L_o = 6$ $\Delta p = 0.66$ [bar], $F_f = 17.31$ [N], $F_{act} = 49.55$ [N]</p>	
<p>Type: Cork, Number: 8 $v_1 = 8.67$, $v_2 = 6.50$, $g_1 = 1.5$, $g_2 = 1.5$, $x = 2$, $\alpha_1 = 30$ [deg], $\alpha_2 = 60$ [deg], $h_{p1} = -1$, $h_{p2} = 3$, $L_i = 10$, $L_a = 18$, $L_o = 5$ $\Delta p = 0.96$ [bar], $F_f = 41.12$ [N], $F_{act} = 81.61$ [N]</p>	
<p>Type: Cork, Number: 9 $v_1 = 8.86$, $v_2 = 5.32$, $g_1 = 1.5$, $g_2 = 1.5$, $x = 1.5$, $\alpha_1 = 30$ [deg], $\alpha_2 = 45$ [deg], $h_{p1} = 0$, $h_{p2} = 2.5$, $L_i = 8$, $L_a = 19$, $L_o = 3$ $\Delta p = 1.79$ [bar], $F_f = 75.31$ [N], $F_{act} = 55.74$ [N]</p>	

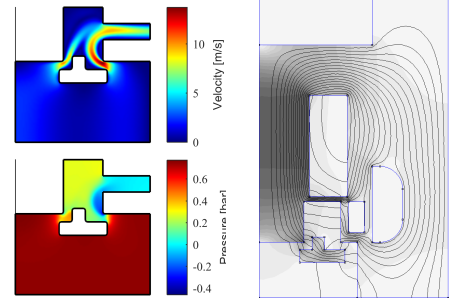
Type: Cork, Number: 10

$$v_1 = 8.13, v_2 = 4.88, g_1 = 1.5, g_2 = 1.5, x = 1, \\ \alpha_1 = 45 [\text{deg}], \alpha_2 = 45 [\text{deg}], h_{p1} = -0.5, h_{p2} = 3, \\ L_i = 7, L_a = 10, L_o = 4 \\ \Delta p = 2.94 [\text{bar}], F_f = 137.52 [\text{N}], F_{act} = 26.93 [\text{N}]$$



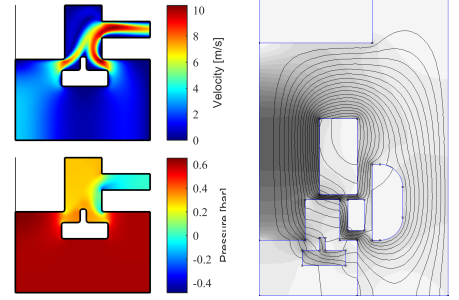
Type: Tap, Number: 1

$$v_1 = 8.13, v_2 = 0.81, v_3 = 1.632, v_4 = 2.44, v_5 = 3.25, v_6 = 0.81, \\ x = 1.5, h_{p1} = 1, h_{p2} = 2.5, \\ L_i = 10, L_a = 10, L_o = 5 \\ \Delta p = 0.75 [\text{bar}], F_f = 39.86 [\text{N}], F_{act} = 61.68 [\text{N}]$$



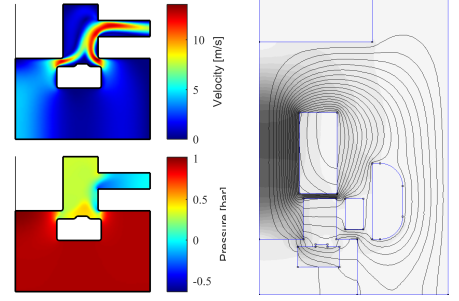
Type: Tap, Number: 2

$$v_1 = 8.60, v_2 = 0.57, v_3 = 2.872, v_4 = 1.15, v_5 = 2.87, v_6 = 1.15, \\ x = 2, h_{p1} = 0.5, h_{p2} = 3, \\ L_i = 12, L_a = 15, L_o = 3 \\ \Delta p = 0.61 [\text{bar}], F_f = 21.34 [\text{N}], F_{act} = 75.69 [\text{N}]$$



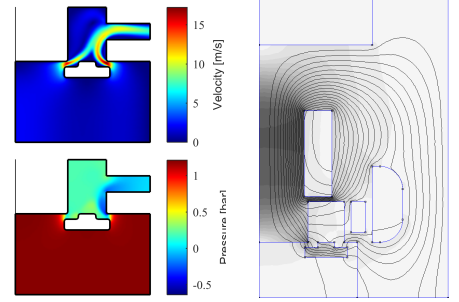
Type: Tap, Number: 3

$$v_1 = 7.68, v_2 = 1.18, v_3 = 2.362, v_4 = 2.36, v_5 = 1.77, v_6 = 0.59, \\ x = 1.5, h_{p1} = -1, h_{p2} = 4, \\ L_i = 8, L_a = 14, L_o = 7 \\ \Delta p = 0.94 [\text{bar}], F_f = 34.11 [\text{N}], F_{act} = 31.76 [\text{N}]$$

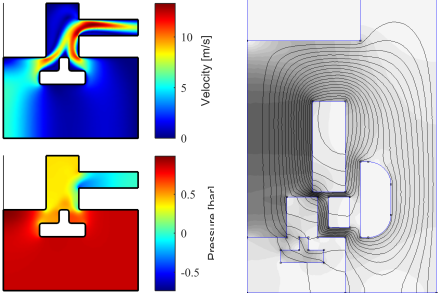
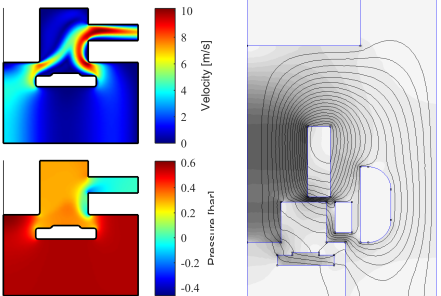
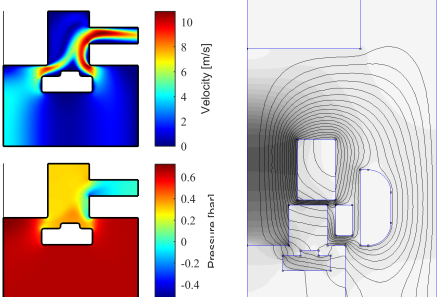
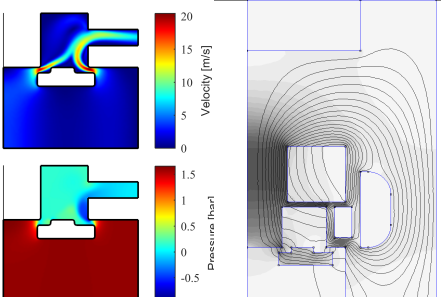


Type: Tap, Number: 4

$$v_1 = 9.10, v_2 = 0.65, v_3 = 1.952, v_4 = 3.25, v_5 = 1.95, v_6 = 0.65, \\ x = 1, h_{p1} = 0, h_{p2} = 2, \\ L_i = 9, L_a = 13, L_o = 8 \\ \Delta p = 1.20 [\text{bar}], F_f = 70.12 [\text{N}], F_{act} = 58.36 [\text{N}]$$



APPENDIX B. TEST POPULATION

<p>Type: Tap, Number: 5 $v_1 = 6.70$, $v_2 = 1.22$, $v_3 = 2.442$, $v_4 = 1.83$, $v_5 = 1.83$, $v_6 = 1.22$, $x = 2.5$, $h_{p1} = 0$, $h_{p2} = 2.5$, $L_i = 13$, $L_a = 12$, $L_o = 3$ $\Delta p = 0.86$ [bar], $F_f = 20.09$ [N], $F_{act} = 42.82$ [N]</p>	
<p>Type: Tap, Number: 6 $v_1 = 6.27$, $v_2 = 0.70$, $v_3 = 2.792$, $v_4 = 3.48$, $v_5 = 1.39$, $v_6 = 0.70$, $x = 1.5$, $h_{p1} = 1.5$, $h_{p2} = 1$, $L_i = 11$, $L_a = 11$, $L_o = 3$ $\Delta p = 1.55$ [bar], $F_f = 64.59$ [N], $F_{act} = 59.26$ [N]</p>	
<p>Type: Tap, Number: 7 $v_1 = 6.00$, $v_2 = 0.75$, $v_3 = 2.252$, $v_4 = 5.25$, $v_5 = 1.50$, $v_6 = 1.50$, $x = 2.5$, $h_{p1} = -2$, $h_{p2} = 2$, $L_i = 12$, $L_a = 16$, $L_o = 6$ $\Delta p = 0.56$ [bar], $F_f = 21.23$ [N], $F_{act} = 53.00$ [N]</p>	
<p>Type: Tap, Number: 8 $v_1 = 7.09$, $v_2 = 1.18$, $v_3 = 2.362$, $v_4 = 3.55$, $v_5 = 1.77$, $v_6 = 0.59$, $x = 2$, $h_{p1} = -1$, $h_{p2} = 3$, $L_i = 10$, $L_a = 18$, $L_o = 5$ $\Delta p = 0.65$ [bar], $F_f = 22.86$ [N], $F_{act} = 66.78$ [N]</p>	
<p>Type: Tap, Number: 9 $v_1 = 6.29$, $v_2 = 0.63$, $v_3 = 1.892$, $v_4 = 4.40$, $v_5 = 2.52$, $v_6 = 1.26$, $x = 1$, $h_{p1} = 0$, $h_{p2} = 2.5$, $L_i = 8$, $L_a = 19$, $L_o = 3$ $\Delta p = 1.61$ [bar], $F_f = 116.48$ [N], $F_{act} = 77.20$ [N]</p>	

Type: Tap, Number: 10

$v_1 = 5.57$, $v_2 = 1.11$, $v_3 = 2.232$, $v_4 = 4.46$, $v_5 = 1.67$, $v_6 = 0.56$,

$x = 1.5$, $h_{p1} = -0.5$, $h_{p2} = 3$,

$L_i = 7$, $L_a = 10$, $L_o = 4$

$\Delta p = 0.99$ [bar], $F_f = 45.09$ [N], $F_{act} = 23.69$ [N]

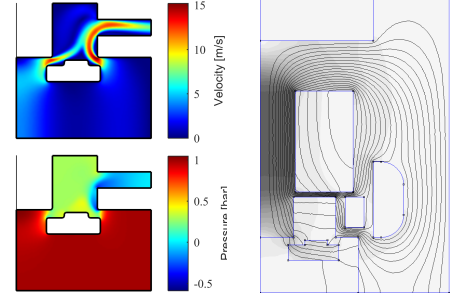


Table B.1: All the designs of the test population. The pressure drop and fluid force are at $120 \text{ [l min}^{-1}\text{]}$, and the actuator force is at 6000 Ampere-turns.